The Astronomical Journal, 125:684–706, 2003 February

VLT/UVES ABUNDANCES IN FOUR NEARBY DWARF SPHEROIDAL GALAXIES. I. NUCLEOSYNTHESIS AND ABUNDANCE RATIOS[1]

Matthew Shetrone
McDonald Observatory, University of Texas, HC75 Box 1337-L, Fort Davis, TX 79734

Kim A. Venn
Macalester College, 1600 Grand Avenue, Saint Paul, MN 55105; University of Minnesota, 116 Church Street, S.E., Minneapolis, MN 55455

Eline Tolstoy
Kapteyn Institute, University of Groningen, P.O. Box 800, NL-9700 AV Groningen, Netherlands

Francesca Primas
European Southern Observatory, Karl-Schwarzschild-Strasse 2, D-85748 Garching bei München, Germany

Vanessa Hill
Observatoire de Paris-Meudon, GEPI, Place Jules Janssen 2, F-92195 Meudon Cedex, France

and

Andreas Kaufer
European Southern Observatory, Alonso de Cordova 3107, Santiago 19, Chile
Received 2002 August 19; accepted 2002 November 5

ABSTRACT

We have used the Ultraviolet Echelle Spectrograph (UVES) on Kueyen (UT2) of the Very Large Telescope to take spectra of 15 individual red giants in the Sculptor, Fornax, Carina, and Leo I dwarf spheroidal galaxies (dSph's). We measure the abundances of α-, iron peak, first *s*-process, second *s*-process, and *r*-process elements. No dSph giants in our sample show the deep mixing abundance pattern (O and sometimes Mg depleted, while Na and Al are enhanced) seen in nearly all globular clusters. At a given metallicity the dSph giants exhibit lower [el/Fe] abundance ratios for the α-elements than stars in the Galactic halo. The low α abundances at low metallicities can be caused by a slow star formation rate and contribution from Type Ia SNe, and/or a small star formation event (low total mass) and mass-dependent Type II SN yields. In addition, Leo I and Sculptor exhibit a declining even-*Z* [el/Fe] pattern with increasing metallicity, while Fornax exhibits no significant slope. In contrast, Carina shows a large spread in the even-*Z* abundance pattern, even over small metallicity ranges, as might be expected from a bursting star formation history. The metal-poor stars in these dSph galaxies ([Fe/H] < -1) have halo-like *s*- and *r*-process abundances, but not every dSph exhibits the same evolution in the *s*- and *r*-process abundance pattern. Carina, Sculptor, and Fornax show a rise in the *s*-/*r*-process ratio with increasing metallicity, evolving from a pure *r*-process ratio to a solar-like *s*- and *r*-process ratio. On the other hand, Leo I, appears to show an *r*-process–dominated ratio over the range in metallicities sampled. At present, we attribute these differences in the star formation histories of these galaxies. Comparison of the dSph abundances with those of the halo reveals some consistencies with the Galactic halo. In particular, Nissen & Shuster found that their metal-rich, high $R_{\rm max}$ high $z_{\rm max}$ halo stars exhibited low [α/Fe], [Na/Fe] and [Ni/Fe] abundance ratios. In the same abundance range our dSph exhibit the same abundance pattern, supporting their suggestions that disrupted dSph's may explain up to 50% of the metal-rich halo. Unfortunately, similar comparisons with the metal-poor Galactic halo have not revealed similar consistencies, suggesting that the majority of the metal-poor Galactic halo could not have been formed from objects similar to the dSph studied here. We use the dSph abundances to place new constraints on the nucleosynthetic origins of several elements. We attribute differences in the evolution of [Y/Fe] in the dSph stars versus the halo stars to a very weak AGB or SN Ia yield of Y (especially compared with Ba). That a lower and flatter Ba/Y ratio is seen in the halo is most likely a result of the pattern being erased by the large metallicity dispersion in the halo. Also, we find [Cu/Fe] and [Mn/Fe] are flat and halo-like over the metallicity city range $-2 <$ [Fe/H] < -1.2, and that the [Cu/α] ratios are flat. Combining these abundances with knowledge of the age spread in these galaxies suggests that SNe Ia are not the main site for the production of Cu (and Mn) in very metal-poor stars. We suggest that metallicity-dependent SN yields may be more promising.

Key words: galaxies: abundances — galaxies: dwarf — galaxies: individual (Sculptor, Fornax, Carina, Leo I) — stars: abundances

On-line material: machine-readable tables

[1] Based on Ultraviolet-Visual Echelle Spectrograph observations collected at the European Southern Observatory, Paranal, Chile, within the observing programs 65.N-0378 and 66.B-0320

1. INTRODUCTION

Hierarchical structure formation models predict that massive galaxies formed through continuous accretion of numerous satellites, a process that, at a lower rate, should be continuing until today. One testable prediction is that the Galactic halo should have been formed through many minor merger events. Another is the number of low-mass satellites that should be observable today around the Galaxy (White & Rees 1978; Moore et al. 1999; Klypin et al. 2002). Indeed both the Galaxy and M31 contain at least one clear remnant of a dwarf galaxy accretion event: The tidal debris of the Sagittarius dwarf spheroidal (dSph) galaxy (Ibata, Gilmore, & Irwin 1994) and a giant stream of metal-rich stars within the halo of M31 (Ibata et al. 2001). Less pronounced streams are more difficult to detect but may stand out kinematically and in terms of abundances (e.g., Helmi et al. 1999). It has also been suggested that the outer halo globular clusters with their predominantly red horizontal branches did not originally form in the Galaxy but were accreted from dwarf satellites (e.g., van den Bergh 2000).

Thus, how did the Galactic halo form, and what role did the accretion of dSph galaxies play? If we consider ages, dSphs can plausibly have contributed significantly to the build-up of the Galactic halo, since the ages of their oldest detectable populations have been found to be indistinguishable from the oldest halo globular clusters within the measurement accuracy. An alternative approach is to accurately *measure* the dSph chemical evolution, as preserved in stellar heavy element abundance patterns, and compare that with the Galactic halo chemical evolution. This has been done for only a small samples of stars in a few nearby dSphs. The chemical evolution picture presented by Shetrone, Côté, & Sargent (2001, hereafter SCS01) is that the metal-poor giants among the smallest dSphs (Draco, Ursa Minor, and Sextans) have an abundance pattern that is *not* consistent with that found in the majority of Galactic halo stars.

Dwarf spheroidal galaxies can also contribute to our understanding of the nucleosynthesis of the elements. The difference in their star formation histories and environments allows us to decouple and test some of the assumptions made in interpreting the Galactic halo abundance patterns. For example, the formation of even-Z elements and r-process elements are assumed to occur in SNe II, while the s-process is thought to originate in AGB stars and iron peak elements from SNe Ia. If the star formation rate, and hence the chemical evolution, is slower in dSph's, then we should see a larger effect of metal-poor SNe Ia and AGB stars than would be seen in the Galactic halo abundance patterns. In addition, because of the isolation of the dSph environment we can test closed-box models of chemical evolution and look for the affects of star formation bursts and a slow star formation. For example, examination of the formation of first and second peak s-process elements (e.g., Y/Ba) are hampered in the halo because of its mixed metallicity population (e.g., see McWilliam 1997). Chemical evolution in the halo occurred very rapidly, and by the time AGB stars begin to contribute to the ISM in the Galactic halo there is a broad range of metallicities ($-3 < [M/H] < -1$) in those AGB stars. Studying Ba and Y abundances in different environments can reveal new constraints on those elements nucleosynthetic origins. As another example of constraining nucleosynthetic origins of different elements, Cu and Mn have been thought to be primarily produced in SNe Ia, since Cu and Mn in the Galactic halo stars mirror the α-element abundances (Matteucci et al. 1993; Samland 1998; Nakamura et al. 1999), and yet other sources for Cu have been discussed in the literature (e.g., Timmes, Woosley, & Weaver 1995). Thus, in the halo stars it is virtually impossible to distinguish SN Ia, from AGB, from metallicity-dependent SN II nucleosynthetic sources, whereas it may be possible to disentangle these sources with dSph abundance patterns.

In this paper we sample four southern dSph galaxies that have not been previously examined: Carina, Fornax, Sculptor, and Leo I. Sculptor has a mean age similar to that of a Galactic globular cluster, but there was probably a spread in age of at least 4 Gyr (e.g., Monkiewicz et al. 1999). From low-resolution spectra Tolstoy et al. (2001) found that Sculptor's mean metallicity was $\langle [Fe/H] \rangle = -1.5$ with a 0.9 dex metallicity spread. Fornax appears to have a highly variable star formation history spanning from $\sim$15 Gyr to 0.5 Gyr ago (e.g., Buonanno et al. 1999). From low-resolution spectra Tolstoy et al. 2001 found that Fornax's mean metallicity was $\langle [Fe/H] \rangle = -1.0$ with a 1.0 dex metallicity spread. Carina exhibits a significant variation in star formation rate with time, with the bulk of the stars having formed 4–7 Gyr ago (e.g., Hurley-Keller, Mateo, Nemec 1998; Dolphin 2002). From low-resolution spectra Da Costa 1984 found that Fornax's mean metallicity was $\langle [Fe/H] \rangle = -1.9$ with a 0.1 dex metallicity spread. Leo I exhibits a significant spread in age, with the bulk of the stars having formed 2–7 Gyr ago (e.g., Gallart et al. 1999; Dolphin 2002). No low-resolution abundance information is available for Leo I. The previous high-resolution surveys (Shetrone, Bolte, & Stetson 1998; SCS01) sampled Ursa Minor, Draco, and Sextans, which have star formation histories similar to Sculptor's, dominated by a single old population. Comparing abundances in dSph with extremely different star formation histories, as well as differences from the Galactic halo, allows us to further examine the nucleosynthetic sources for a variety of interesting elements.

2. OBSERVATIONS

Spectra of red giants in four dSph's were obtained at the Very Large Telescope Kueyen at Paranal, Chile, in 2000 August and 2001 January using the Ultraviolet-Visual Echelle Spectrograph (UVES, Dekker et al. 2000) in visitor mode (see Table 1). The red arm of UVES with CD No. 3 was centered at 580 nm, and with a 1.″0 slit we obtained a resolution $\sim$40,000 (4.4 pixels) over a wavelength range of 480–680 nm. The total integration time varied from 2–4 hr (1 hr per exposure), depending on the brightness of the target and the sky conditions. Monodimensional spectra were extracted with the UVES pipeline (Ballester et al. 2000), then continuum-normalized and combined with IRAF for a S/N $\sim$ 30 pixel^{-1}.

A variety of elements were detected in the spectra, including Fe, O, Na, Mg, Al, Ca, Sc, Ti, Cr, Ni, Y, Ba, Nd, La, and Eu. This allowed for a comprehensive abundance analysis (e.g., Kraft et al. 1992, 1993). Four red giants in clusters of known metallicity (see Table 2) were observed as standard stars to establish the abundance scale. Analysis of these stars allowed us to look for zero-point offsets and place our abundances on a standard system.

TABLE 1

OBSERVATIONS

Date	Begin (UT)	Object	Exp. (s)	Air Mass	DIMM[a] (arcsec)	Comments
2000 Aug 16	04:24	Scl H461	3600	1.36	0.92	
2000 Aug 16	05:26		3600	1.15	0.98	
2000 Aug 16	06:29		3600	1.05	0.66	
2000 Aug 16	07:34	Scl H400	1945	1.02	0.46	Tracking
2000 Aug 16	09:03		3600	1.09	0.55	
2000 Aug 17	04:53		3600	1.23	0.58	
2000 Aug 17	05:56		3600	1.09	0.56	
2000 Aug 18	04:18	Scl H479	3600	1.35	0.54	
2000 Aug 18	05:20		3600	1.15	0.53	
2000 Aug 19	03:24	Scl H482	1800	1.80	0.45	
2000 Aug 19	03:56		1800	1.50	0.44	
2000 Aug 19	04:30		3600	1.28	0.45	
2000 Aug 19	05:35	Scl H459	3600	1.11	0.32	
2000 Aug 19	06:37		3402	1.03	0.29	Tracking
2000 Aug 19	09:06		3600	1.11	0.85	
2000 Aug 17	07:04	Fnx M22	2068	1.17	0.82	C-star
2000 Aug 17	08:58	Fnx M12	1273	1.02	0.70	Tracking
2000 Aug 18	06:26		3600	1.24	0.53	
2000 Aug 18	07:28		4500	1.09	0.47	
2000 Aug 18	08:44		1890	1.02	0.43	Tracking
2000 Aug 18	09:29		1800	1.02	0.43	
2000 Aug 19	07:58	Fnx M25	3600	1.05	0.57	
2000 Aug 20	07:45		3600	1.06	0.85	
2000 Aug 20	08:47		3600	1.02	1.08	
2000 Aug21	09:16		3200	1.02	0.84	
2000 Aug 20	09:51	Fnx M21	1200	1.03	0.99	
2000 Aug 22	07:09		3200	1.10	0.74	
2000 Aug 22	08:10		3600	1.03	0.89	
2000 Aug 22	09:12		2382	1.02	0.79	Tracking
2000 Aug 22	09:55		572	1.03	0.80	Twilight
2000 Aug 17	04:15	M30 D	600	1.00	0.49	
2000 Aug 17	04:34	M55 76	300	1.12	0.42	
2000 Aug 17	04:40		300	1.13	0.49	
2000 Aug 18	23:17	M55 283	300	1.35	0.46	
2000 Aug 18	23:23		300	1.33	0.48	
2000 Jan 17	02:07	Car 12	3600	1.15	0.42	
2000 Jan 17	03:11		3600	1.12	0.47	
2001 Jan 17	04:17	Car 2	3600	1.16	0.61	
2001 Jan 17	05:18		3600	1.25	0.62	
2000 Jan 18	01:31	Car 4	3600	1.18	[b]	
2000 Jan 18	02:33		3600	1.13	[b]	
2000 Jan 18	03:39	Car 10	3600	1.13	[b]	
2000 Jan 18	04:41		3600	1.19	0.46	
2000 Jan 19	00:19	Car 3	1200	1.37	0.76	
2000 Jan 19	02:33		3600	1.13	0.76	
2000 Jan 19	03:34		2700	1.12	0.67	
2000 Jan 17	06:24	Leo I 2	3600	1.26	0.57	
2000 Jan 17	07:24		4500	1.32	0.61	
2000 Jan 18	05:48		4500	1.29	[b]	
2000 Jan 19	08:04		3400	1.41	0.50	
2000 Jan 18	07:10	Leo I 24	3100	1.28	[b]	C-star
2000 Jan 18	08:23	Leo I 5	1800	1.40	0.51	
2000 Jan 19	04:25		3600	1.49	0.64	
2000 Jan 19	05:27		4500	1.31	[b]	
2000 Jan 19	06:44		4500	1.28	[b]	
2000 Jan 17	08:46	M68 53	300	1.02	0.66	
2000 Jan 17	08:52		300	1.01	0.57	

[a] This is just an indication of the external seeing measured automatically by the seeing monitor (DIMM) on the mountain. Usually the seeing on the instrument is better than this.

[b] DIMM was not working for a short period.

TABLE 2
THE STELLAR SAMPLE

Galaxy	Star ID	V	$(B-V)_0$	$(V-I)_0$	RV_{helio} (km s^{-1})	Ref.
Sculptor	H400	18.30	0.89	1.04	109	1, 2, 11, 12
	H459	18.14	1.03	1.16	116	
	H461	17.56	1.17	1.35	104	
	H479	17.23	1.20	1.31	98	
	H482	17.65	1.21	1.41	107	
Fornax	M12	18.43	1.33	1.50	54	3, 11, 12
	M25	18.59	1.49	1.53	49	
	M21	18.37	1.59	1.66	53	
Carina	M2	17.68	1.325	...	221	4, 11, 12
	M3	17.75	1.415	1.32	227	
	M4	17.81	1.285	1.28	221	
	M10	18.09	1.255	...	210	
	M12	18.08	1.185	1.19	217	
Leo I	M2	19.37	...	1.34	292	5, 11, 12
	M5	19.37	...	1.44	304	
MW M55	76	12.55	0.85	...	175	6, 7, 8
	283	12.75	1.01	...	172	6, 7, 8
MW M30	D	12.81	1.00	...	−186	6, 9
MW M68	53	12.76	1.22	...	−96	10

REFERENCES.—(1) Hodge 1965; (2) Queloz, Dubath, & Pasquini 1995; (3) Mateo et al. 1991; (4) Mateo et al. 1993; (5) Mateo et al. 1998; (6) Harris 1996, (7) Harris 1975, (8) Alcaino 1975, (9) Alcaino & Liller 1980; (10) Alcaino 1977; (11) Paper II; (12) $E(V-I)$ from Dean, Warren, & Cousins 1978.

3. DATA REDUCTION AND EW MEASUREMENT

Radial velocities for each red giant (see Table 2) were measured from three metal lines (Fe I λ5083.35, Ca I λ6122.23, and Ba II λ6141.73) and two Balmer lines (Hα and Hβ). Heliocentric corrected radial velocities are listed in Table 2. The radial velocities were used to ascertain galaxy membership, and all are in excellent agreement with published values (see the references in Table 2).

Equivalent widths were measured three different ways using the IRAF task SPLOT. The first strategy was an integrated flux method (Simpson's rule), the second was a normal Gaussian fit, the third was using multiple Gaussians for lines that appeared asymmetric or blended with other lines. In the latter cases the Gaussian FHWMs were forced to be the same for all components. When the lines were not asymmetric, EWs were adopted from the integrated flux method, unless a bad pixel in the line profile made the Gaussian-fit method preferable. The adopted EWs are reported in Tables 3 and 4.

Figure 1 shows a comparison of the EW measured here and those measured for the GC sample from Minniti et al. 1993. There is no systematic trend or offset for the entire sample. The standard deviation of the entire sample is 11.5 mÅ; however, the differences are slightly higher at larger EWs, which we attribute to a small error that scales with EW. We adopt the errors Minniti et al. use for their EW, 6 mÅ, as the minimum EW measurement error. This uncertainty is shown

TABLE 3
EQUIVALENT WIDTHS AND ATOMIC DATA

Elem.	λ (Å)	χ (eV)	log gf	M30 D	M55 283	M55 76	M68 53	Scl H400	Scl H459	Scl H461	Scl H479	Scl H482
Fe I	4966.10	3.33	−0.890	66	88	84	74	...	...	...	...	...
	5006.12	2.83	−0.628	108	124	123	116	106	131	129	...	153
	5079.75	0.99	−3.240	116	125	...	136	...	...	...	...	174
	5083.35	0.96	−2.862	125	125	128	137	127	138	155	154	179
	5150.85	0.99	−3.030	115	127	121	129	103	134	145	158	169
	5151.92	1.01	−3.326	108	110	111	118	92	121	137	124	171
	5159.05	4.28	−0.810	14	25	19	17	...	29	32	42	52
	5162.29	4.18	0.020	55	84	71	68	72	83	96	80	100
	5165.41	4.22	−0.040	...	...	...	...	...	75	...	...	...
	5166.28	0.00	−4.200	140	132	137	160	122	160	...	...	181

NOTE.—Table 3 is presented in its entirety in the electronic version of the Astronomical Journal. A portion is shown here for guidance regarding its form and content.

[a] Hyperfine structure references: Cu I, Biehl 1976; Mn I, Booth et al. 1983; La II, Lawler, Bonvallet, & Sneden 2001a; Ba II, McWilliam 1998; Eu II, Lawler et al. 2001b.

TABLE 4
EQUIVALENT WIDTHS AND ATOMIC DATA

Elem.	λ (Å)	χ (eV)	log *gf*	Car 10	Car 12	Car 2	Car 3	Car 4	Fnx M12	Fnx M21	Fnx M25	Leo 2	Leo 5
Fe I.....	4966.10	3.33	−0.890	93	136	...	...	130	130	...	...	...	...
	5006.12	2.83	−0.628	137	169	162	172	...	...	...	202	193	180
	5079.75	0.99	−3.240	...	...	173	...	...	...	...	...	...	...
	5083.35	0.96	−2.862	152	186	193	198	195	...	...	241	210	...
	5150.85	0.99	−3.030	144	186	186	181	200	...	...	211	199	198
	5151.92	1.01	−3.326	139	176	180	188	170	...	...	...	...	...
	5159.05	4.28	−0.810	26	57	56	37	57	39	...	69	67	62
	5162.29	4.18	0.020	78	118	112	106	112	95	...	120	...	134
	5165.41	4.22	−0.040	...	98	86	68	...	...	...	...	...	...
	5166.28	0.00	−4.200	167	201	216	217	217	...	...	...	...	206

NOTE.—Table 4 is presented in its entirety in the electronic version of the Astronomical Journal. A portion is shown here for guidance regarding its form and content.

[a] Hyperfine structure references: Cu I, Biehl 1976; Mn I, Booth et al. 1983; La II, Lawler et al. 2001a; Ba II, McWilliam 1998; Eu II, Lawler et al. 2001b.

by the dotted lines in the top plot of Figure 1. The dashed lines represent a combination of this minimum uncertainty, plus a 10% × EW uncertainty that is added in quadrature. We will use this additional 10% × EW uncertainty later in our error analysis. When each star is examined separately, there do appear to be some systematic differences. For example, our EWs for M55 283 tend to be slightly lower than those from Minniti et al. (1993), although still in agreement to within 10%. We attribute these small systematic differences to the choice of continuum normalization.

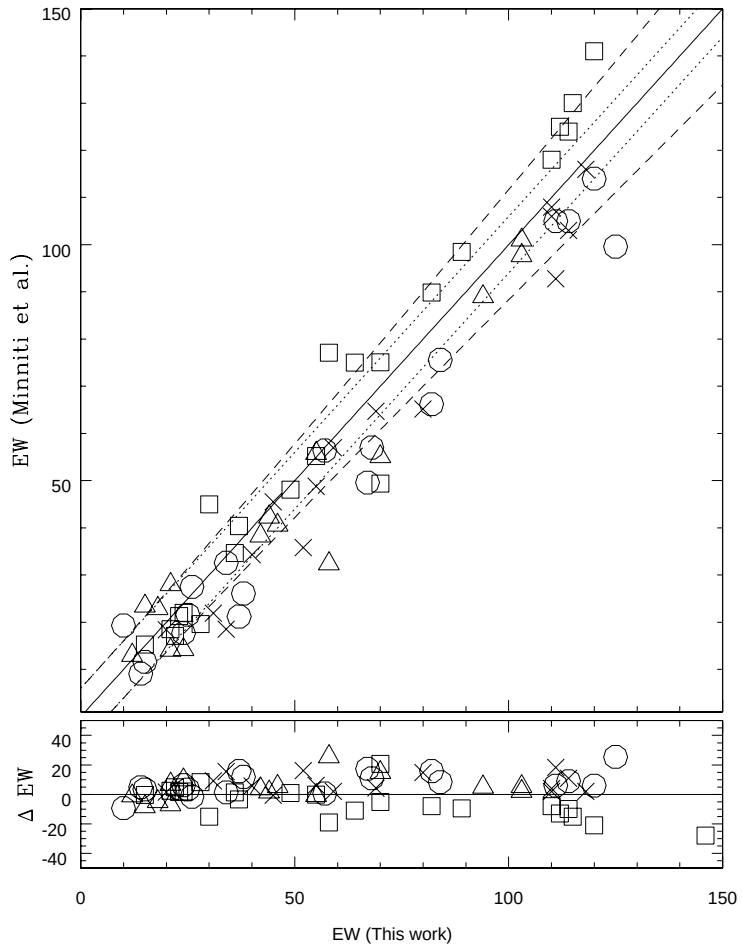

FIG. 1.—Comparison the EW from this work and Minniti et al. 1993. The triangles represent M30 D lines, the squares M55 283 lines, the crosses M55 76 lines, and the circles M68 53 lines. The solid line is the 45° line. The dotted line is offset from the 45° line by an error of 6 mÅ. The dashed line represents a 10% error convolved with the 6 mÅ error.

4. OSCILLATOR STRENGTHS

Most of the oscillator strengths adopted in this work were taken from the Lick-Texas papers (e.g., Kraft et al. 1992 and Sneden et al. 1991) as summarized in Shetrone et al. (1998) and SCS01, and also from Fulbright (2000). These lines were selected for accurate abundances in metal-poor giants. Because several of the dSph giants in this paper are very metal-rich, than additional lines were added from Edvardsson et al. (1993). In addition, UVES on the VLT has a larger spectral coverage than HIRES on Keck, which allowed us to add more lines. Atomic data for these lines was obtained from the National Institute of Standards and Technology on-line Atomic Spectra Database.[2]

4.1. *HFS Lines*

Hyperfine structure (HFS) plays a role in a number of elements analyzed in this work, including Eu, Ba, Cu and Mn. The parameters for the HFS were taken from a number of different references, as noted in Tables 3 and 4. HFSs for Eu were taken from Lawler et al. (2001b), but for consistancy we have continued to use oscillator strength from SCS01. Adopting the Lawler et al. (2001b) oscillator strength would shift our Eu abundances up by 0.08 dex. Using the slightly higher solar abundance in Lawler et al. (2001b) would reduce this to 0.07 dex offset.

The HFS analysis was examined in all stars, but for weak lines (<40 mÅ) of Cu, La, and Eu the HFS corrections were insignificant. For the star with the strongest Eu line (Fnx 21, 87 mÅ) the HFS correction was 0.23 dex, for all other stars the HFS correction is less than 0.12 dex. For the Ba lines used in this analysis, the HFS corrections and isotope splitting made no significant differences to the abundances, even for the strongest lines. Only for the Mn lines were the HFS corrections significant for all lines (EW > 30 mÅ).

5. ANALYSIS

Model atmospheres were taken from the computations of the MARCS code (Gustafsson et al. 1975), and the abundance calculations were performed using the 2000 December 19 version of Sneden's (1973, MOOG) LTE line analysis and spectrum synthesis code. The procedures are identical to those employed in SCS01, ensuring that the relative abundance and model parameter scales should be similar. In general, a color temperature and metallicity were adopted per program star (discussed below), and the initial temperature was adjusted to minimize the slope in Fe abundance (from Fe I) versus excitation potential. Minimizing the slope between Fe I line abundances and their equivalent widths also provided the microturbulent velocity. Following this, the surface gravity was determined by requiring that the abundance of the *ionized* species equal that of the *neutral* species based on Fe I and Fe II. These steps usually required a few iterations before the parameters converged and were adopted for the abundance analysis. Model atmospheres are from the MARCS grid that are slightly more metal-rich than the actual derived abundances to compensate for the extra electrons that are contributed by α-rich metal-poor stars (see Fulbright & Kraft 1999 for more about this methodology). Model atmosphere parameters determined here are listed in Table 5.

[2] Available at http://physics.nist.gov/cgi-bin/AtData/main_asd.

TABLE 5
ATMOSPHERIC PARAMETERS

OBJ	$T_{\rm eff}$ (K)	log g	ξ (km s^{-1})	[Fe I/H]
M30 D	4400	0.50	2.0	−2.30
M55 283	4600	1.20	1.65	−1.75
M55 76	4550	0.90	1.9	−1.99
M68 53	4300	0.30	2.0	−2.21
Scl 400	4650	0.90	1.7	−1.98
Scl 459	4500	1.00	1.65	−1.66
Scl 461	4500	1.20	1.7	−1.56
Scl 479	4325	0.70	1.7	−1.77
Scl 482	4400	1.10	1.7	−1.24
Fnx 25	4025	0.00	2.0	−1.21
Fnx 12	4150	0.00	2.1	−1.60
Fnx 21	4000	0.50	1.7	−0.67
Leo 2	4200	0.50	1.85	−1.06
Leo 5	4250	0.80	2.2	−1.52
Car 2	4250	0.55	2.1	−1.60
Car 3	4250	0.20	2.2	−1.65
Car 4	4200	0.40	2.1	−1.59
Car 10	4375	0.40	2.0	−1.94
Car 12	4300	0.60	1.9	−1.41

In addition, we performed two checks on our model atmospheres analyses. First, the final model temperatures were examined relative to the initial color temperatures derived from the $B-V$ colors. Second, the iron (and other) abundances for two stars were also analyzed using ATLAS9 model atmospheres (Kurucz 1993) in WIDTH9 with oscillator strengths from the VALD database (Kupka et al. 1999). The two tests are discussed separately below.

The $B-V$ color for each star provided an initial estimate for the stellar parameters. The conversion from color to stellar parameters was made using a calibration based on the derived parameters for a number of globular cluster stars (Lick-Texas papers: Kraft et al. 1992, 1993, 1995, 1997; Sneden et al. 1991, 1997). Initial estimates were made by assuming a metallicity for each program star based on their location in the color magnitude diagrams, then these estimates were adjusted for the metallicities actually determined per star. Because the iterative nature of our analysis the final temperatures and surface gravities do not match the initial estimates. On average the temperatures differed little from the initial estimates ($\Delta T = -3$ K, $\sigma = 92$ K), while the final surface gravities are a bit lower than the initial estimates ($\Delta \log g = -0.29$ dex, $\sigma = 0.17$ dex). Colors were taken from Schweitzer et al. 1995 (for Sculptor), Mateo et al. 1991 (for Fornax), Mateo et al. 1993 (for Carina), and Mateo et al. 1998 (for Leo I). Reddening estimates were taken from Kaluzny et al. 1995 (for Sculptor), Schlegel, Finkbeiner, & Davis 1998 (for Fornax), Mould & Aaronson 1983 (for Carina), and Cardelli, Clayton, & Mathis 1989 (for Leo I). A second check of our adopted stellar parameters was performed using the the Alonso temperature scale (see Table 2 in Alonso, Arribas, Martínez-Roger 1999) and then using that effective temperature and the new Yale-Yonsei isochrones (Yi et al. 2001; Green, Demarque, & King 1987) to derive surface gravity. The Alonso temperature scale (making the correction in Alonso et al. 2001) and literature B-V colors suggest a slightly cooler temperature than our adopted temperatures ($\Delta T = +60$ K, $\sigma = 107$ K); however, the surface gravities based on the isochrones is in good

agreement with our adopted gravities ($\Delta \log g = -0.07$ dex, $\sigma = 0.18$ dex). Tolstoy et al. (2003, hereafter Paper II) use Cousins *I*, while the Alonso temperature scale uses Johnson *I*. Using Bessell (1986, 1990) to convert the colors and converting the $E(B-V)$ to $E(V-I)$ using Dean, Warren, & Cousins 1978, we find a similar zero point ($\Delta T = +51$ K, $\sigma = 131$ K) between our derived temperatures and the Alonso temperature scale. The large dispersion in both $V-I$ and $B-V$ could be due to variable reddening. Inspection of the spectra reveals a factor of 2 dispersion in EW of the interstellar Na D lines among the Carina sample. As mentioned before, we have adopted the spectroscopic temperatures and have only used the photometric temperatures as an initial estimate and a secondary check on our methodology.

Two stars, the cluster star M55 76 and the Sculptor star Scl 459, were checked with ATLAS9/WIDTH9 calculations and VALD atomic data. The abundances for Fe I and Fe II lines are in very good agreement ($\Delta \log (X/H) \leq 0.1$), and most of the iron line abundance disagreements can be traced primarily to small differences in the oscillator strengths. We note, however, that the mean differences go in opposite directions for Fe I and Fe II, so that the ATLAS/WIDTH results do not maintain the iron ionization equilibrium when the MARCS/MOOG parameters are adopted. For example, when Fe I = Fe II using MARCS/MOOG, then the ATLAS/WIDTH/VALD results are Fe I + 0.1 dex = Fe II − 0.1 dex, resulting in a 0.2 dex difference between iron from the Fe I versus the Fe II lines. This will affect the model atmosphere parameters; primarily it will force a higher gravity determination in the ATLAS/WIDTH analysis. While gravity has a very small effect on the Fe I abundances (see Table 6) and thus on the overall metallicity adopted for that model, it can have a larger effect on the abundances of ionized species and also the O I abundance. This is discussed further in § 6.3. Additionally, we stress that the MARCS/MOOG analysis is the most consistent with the published abundances for the globular cluster standard stars and for red giants in other dwarf spheroidal galaxies; thus, we consider these the most appropriate for differential comparisons.

6. ERROR ANALYSIS

We divide our errors into three types: statistical, internal, and external. Statistical uncertainties are those errors which can be reduced by using many lines to measure the abundances. The internal errors are those errors based on analysis methodology, such as derivation of $T_{\rm eff}$ or normalization of the continuum. The external errors are those based on the analysis tools, such as the model atmosphere grid and LTE abundance analysis code.

6.1. *Statistical Errors*

The statistical errors are determined from the consistency of the abundances derived from each line. Assuming that our derived stellar parameters are approximately correct, the variance in the abundance derived for elements with many lines, such as Fe I, is a measure of our ability to measure consistent EWs and the accuracy of our atomic physics inputs (largely, the oscillator strengths and hyperfine structure). Using the Cayrel (1988) formalism, we estimate that our random error in EW should be 4 mÅ for the dSph stars. The Cayrel formalism simply assumes a line profile affected simply by the S/N (30 in our case) and the number of pixels in the resolution element (4 pixels and $R = 40{,}000$). For the weakest lines (∼10 mÅ), this will introduce an uncertainty of 0.19 dex. For moderately strong lines (∼60 mÅ), the uncertainty is 0.03 dex, while for very strong lines (∼150 mÅ), it is only 0.01 dex. The globular cluster spectra have much higher S/N; thus, they will also have smaller EW errors. As mentioned earlier in our comparison of our EW

TABLE 6
ABUNDANCE UNCERTAINTIES FOR CAR 2

Elem.	$\Delta T_{\rm eff}$ (−100 K)	$\Delta \log g$ (−0.2)	$\Delta\xi$ (−0.2 km s^{-1})	[M/H] (−0.15)	Cont. (4 mÅ)	$\Delta T_{\rm eff}$, $\Delta \log g$, $\Delta\xi$ (−100, −0.25, −0.1)
[Fe I/H]	−0.11	+0.02	+0.11	+0.02	−0.06	−0.05
[Fe II/H]	+0.10	−0.07	+0.05	−0.03	−0.08	+0.03
[O I/Fe I]	+0.11	−0.11	−0.11	−0.07	−0.01	−0.05
[Na I/Fe I]	+0.02	+0.01	−0.10	+0.00	−0.02	+0.00
[Mg I/Fe I]	+0.03	+0.03	−0.03	+0.01	+0.01	+0.05
[Si I/Fe I]	+0.11	−0.02	−0.11	−0.02	−0.09	+0.04
[Ca I/Fe I]	−0.03	+0.01	−0.03	+0.01	+0.00	−0.01
[Sc II/Fe I]	+0.13	−0.09	−0.10	−0.06	−0.02	−0.02
[Ti I/Fe I]	−0.10	+0.01	−0.04	+0.01	−0.01	−0.08
[Ti II/Fe I]	+0.13	−0.06	+0.01	−0.04	−0.01	+0.08
[Cr I/Fe I]	−0.10	+0.03	+0.04	+0.01	+0.01	−0.02
[Mn I/Fe I]	−0.06	+0.01	−0.06	+0.01	+0.00	−0.07
[Ni I/Fe I]	+0.02	−0.01	−0.04	+0.02	−0.02	−0.01
[Cu I/Fe I]	+0.05	+0.00	−0.05	+0.02	−0.01	−0.04
[Zn I/Fe I]	+0.18	−0.02	−0.04	−0.02	−0.02	+0.17
[Y II/Fe I]	+0.12	−0.05	−0.01	−0.04	+0.03	+0.06
[Ba II/Fe I]	+0.09	−0.09	+0.08	−0.06	+0.00	+0.04
[Nd II/Fe I]	+0.10	−0.07	−0.05	−0.04	+0.00	+0.00
[La II/Fe I]	+0.10	−0.09	−0.10	−0.04	−0.04	−0.05
[Eu II/Fe I]	+0.12	−0.10	−0.10	−0.06	−0.07	−0.03

NOTE.—The last column is the abundance uncertainty when $T_{\rm eff}$ is changed by −100 K *and* the corresponding changes that would occur in log *g* and microturbulence are taken into account holistically.

to the Minniti et al. (1993) EW, our errors were better represented by a constant with a 10% × EW additional error. Thus, we take our actual error to be 4 mÅ + (10% × EW) in the case for the dSph sample).

Since many elemental abundances are derived from only a few lines, the statistical error is rarely accurately sampled. Thus, we assume that the standard deviation of the Fe I line abundances is typical for most elements. We will refer to this σ as the *average line deviation*. For each element we take the larger of either (1) the standard deviation of the mean of the lines for that element, assuming that there is more than one line, (2) the average line deviation divided by the square root of the number of lines used to determine the abundance for that element, or (3) for elements with only one line the error based just on EW, using the Cayrel formalism plus the (10% × EW) additional error we described earlier.

In Tables 7–10 we have given the abundances and internal statistical error for each element. For Fe I we have listed the number of lines that went into the calculation of the standard deviation of the mean. For the other elements a letter tag is given which represents which method is used. An S means that the standard deviation was taken from that element. An I means that the average line deviation method was used. An E means that the error is derived from the EW error. No uncertainty is given if only an upper limit to the abundance is determined.

6.2. *Internal Errors*

In § 5 we computed the difference between our derived stellar parameters and those based on photometry. From that analysis we adopt internal uncertainties of ±100 K and ±0.2 dex for $T_{\rm eff}$ and log g, respectively. We also estimate that the error in the microturbulent velocity is ±0.2 km s^{-1}. Table 6 lists these effects on the abundances for one star, Car 2, by recomputing the abundances for models with slightly different parameters. We have also listed the effect of choosing a slightly more metal-poor model (i.e., one without the extra metallicity, which compensates for the α-rich abundance pattern), and the effects of shifting the continuum systematically up such that all of the EW are 4 mÅ larger. This continuum error assumes that the line profile width does not grow significantly with EW. This is clearly not true for the very large EW lines, but we have made some effort to remove all strong lines from this analysis, so to first approximation this is a reasonable assumption. For the globular cluster stars the S/N is much higher, and thus we adopt a smaller error in the continuum.

It should be noted that many of these errors are not independent; e.g., a change in the $T_{\rm eff}$ by 100 K introduces a slope in the Fe I line abundances versus the EW plot, which is used to determine the microturbulent velocity. A 100 K change in the $T_{\rm eff}$ also upsets the balance of the Fe I versus Fe II abundances. The last column in Table 6 shows how the abundances would change if we attempted to mediate the effects by recomputing the abundances with a model that was 100 K too cool. We adopt this last column as representing the most accurate abundance error based on changes in $T_{\rm eff}$, log g, and microturbulence.

To combine the uncertainties per element due to the stellar parameters, continuum placement, and metallicity, we have taken these uncertainties in Table 6 and combined

TABLE 7
GLOBULAR CLUSTER STAR ABUNDANCES

Elem.	Sun[a]		M30 D AVG (Δ_r)	M68 53 AVG (Δ_r)	M55 76 AVG (Δ_r)	M55 283 AVG (Δ_r)
Fe	7.52	[Fe I/H]	−2.30 (0.01) 62	−2.21 (0.02) 69	−1.99 (0.01) 65	−1.75 (0.02) 71
		[Fe II/H]	−2.32 (0.04)S	−2.24 (0.04)S	−1.98 (0.03)I	−1.77 (0.04)S
O	8.83	[O I/Fe I]	+0.26 (0.11)I	+0.19 (0.10)I	+0.48 (0.08)I	−0.22 (0.13)I
Na	6.33	[Na I/Fe I]	+0.27 (0.08)I	+0.21 (0.10)S	−0.10 (0.09)S	+0.12 (0.08)I
Mg	7.58	[Mg I/Fe I]	+0.52 (0.09)S	+0.50 (0.11)S	+0.54 (0.10)S	+0.11 (0.11)S
Al	6.47	[Al I/Fe I]	+1.13 (0.08)E	...	<+0.38	+1.15 (0.09)I
Si	7.55	[Si I/Fe I]	+0.50 (0.11)I	+0.66 (0.13)S	+0.49 (0.11)S	+0.42 (0.10)S
Ca	6.36	[Ca I/Fe I]	+0.36 (0.04)S	+0.29 (0.05)I	+0.38 (0.05)S	+0.30 (0.04)I
Sc	3.10	[Sc II/Fe I]	−0.14 (0.11)I	−0.02 (0.14)I	...	−0.20 (0.13)I
Ti	4.99	[Ti I/Fe I]	+0.15 (0.05)S	+0.08 (0.05)I	+0.11 (0.04)I	+0.10 (0.06)S
		[Ti II/Fe I]	+0.23 (0.09)S	+0.14 (0.07)S	+0.26 (0.10)S	+0.17 (0.07)S
Cr	5.67	[Cr I/Fe I]	−0.25 (0.08)I	−0.32 (0.10)I	−0.09 (0.08)I	−0.08 (0.13)I
Mn	5.39	[Mn I/Fe I]	−0.45(0.10)S	−0.48 (0.10)I	−0.48 (0.06)I	−0.38 (0.13)S
Co	4.92	[Co I/Fe I]	+0.18 (0.11)I	+0.18 (0.14)I	+0.30 (0.11)I	...
Ni	6.25	[Ni I/Fe I]	+0.01 (0.11)I	−0.04 (0.14)I	−0.01 (0.08)I	−0.01 (0.13)I
Cu	4.21	[Cu I/Fe I]	−0.68 (0.11)I	−0.78 (0.14)I	−0.74 (0.11)I	−0.87 (0.13)I
Zn	4.60	[Zn I/Fe I]	+0.14 (0.11)I	−0.09 (0.14)I	+0.17 (0.11)I	+0.03 (0.13)I
Y	2.24	[Y II/Fe I]	−0.39 (0.06)I	−0.65 (0.07)I	−0.22 (0.06)I	−0.28 (0.09)I
Ba	2.13	[Ba II/Fe I]	−0.29 (0.11)S	−0.29 (0.08)I	+0.32 (0.06)I	+0.32 (0.08)I
Nd	1.50	[Nd II/Fe I]	−0.11 (0.08)I	−0.10 (0.10)I	+0.18 (0.08)I	+0.22 (0.13)I
La	1.22	[La II/Fe I]	−0.14 (0.17)E	+0.04 (0.17)S	+0.24 (0.11)I	+0.08 (0.08)I
Eu	0.51	[Eu II/Fe I]	+0.24 (0.11)I	+0.12 (0.14)I	+0.59 (0.11)I	+0.48 (0.13)I

NOTES.—The errors quoted here represent only the random errors. These are computed by one of three methods (see text): I: this random error assumes that the random error of the lines of this species behave in a way similiar to those of Fe I ($\sigma_{\rm Fe}/\sqrt{N}$). S: this random error is based on the standard deviation of the abundance of this species ($\sigma_{\rm el}/\sqrt{N}$). E: this random error is based on an error computed from the suggested EW error for the these lines. See Cayrel 1988. For iron, the number of lines used to compute the standard deviation of the mean is given.

[a] Solar abundances are from Grevesse & Sauval 1998.

TABLE 8
CARINA ABUNDANCES

Elem.	Sun		Car 4 AVG (Δ_r)	Car 3 AVG (Δ_r)	Car 2 AVG (Δ_r)	Car 12 AVG (Δ_r)	Car 10 AVG (Δ_r)
Fe	7.52	[Fe I/H]	−1.59 (0.02) 71	−1.65 (0.02) 74	−1.60 (0.02) 74	−1.41 (0.02) 75	−1.94 (0.02) 66
		[Fe II/H]	−1.60 (0.05)S	−1.63 (0.04)I	−1.61 (0.04)I	−1.38 (0.04)S	−1.94 (0.04)I
O	8.83	[O I/Fe I]	+0.22 (0.09)I	+0.04 (0.12)I	+0.44 (0.12)S	+0.17 (0.10)I	+0.08 (0.19)I
Na	6.33	[Na I/Fe I]	−0.35 (0.08)I	−0.58 (0.17)I	−0.38 (0.10)I	−0.26 (0.11)S	−0.66 (0.15)I
Mg	7.58	[Mg I/Fe I]	+0.26 (0.09)S	−0.27 (0.12)I	+0.23 (0.10)I	+0.24 (0.10)I	+0.06 (0.11)I
Al	6.47	[Al I/Fe I]	+0.20 (0.13)I	<+0.27	<+0.24	+0.03 (0.16)E	...
Si	7.55	[Si I/Fe I]	+0.25 (0.06)S	−0.28 (0.17)I	+0.18 (0.07)I	+0.22 (0.07)S	+0.38 (0.22)I
Ca	6.36	[Ca I/Fe I]	+0.14 (0.04)I	−0.10 (0.06)I	+0.20 (0.05)I	+0.12 (0.05)I	−0.02 (0.05)I
Sc	3.10	[Sc II/Fe I]	−0.29 (0.13)I	−0.71 (0.17)I	−0.19 (0.14)I	+0.03 (0.14)I	+0.05 (0.15)I
Ti	4.99	[Ti I/Fe I]	+0.03 (0.04)I	−0.41 (0.07)I	+0.07 (0.05)I	+0.04 (0.05)S	+0.11 (0.05)I
		[Ti II/Fe I]	+0.01 (0.08)S	−0.13 (0.08)I	+0.05 (0.08)S	+0.04 (0.07)S	+0.16 (0.06)I
Cr	5.67	[Cr I/Fe I]	−0.11 (0.16)S	+0.20 (0.12)I	+0.12 (0.10)I	−0.01 (0.11)S	−0.19 (0.11)I
Mn	5.39	[Mn I/Fe I]	−0.32 (0.06)I	−0.44 (0.08)I	−0.33 (0.06)I	−0.32 (0.06)I	−0.42 (0.09)S
Co	4.92	[Co I/Fe I]	+0.10 (0.12)S	−0.08 (0.17)I	...	+0.07 (0.14)S	−0.16 (0.15)I
Ni	6.25	[Ni I/Fe I]	−0.04 (0.07)I	−0.07 (0.10)I	−0.15 (0.08)I	−0.06 (0.08)I	−0.08 (0.15)I
Cu	4.21	[Cu I/Fe I]	−0.63 (0.12)I	−0.85 (0.12)I	−0.63 (0.08)I	−0.61 (0.14)I	<−0.60
Zn	4.60	[Zn I/Fe I]	−0.10 (0.13)I	−0.30 (0.17)I	+0.04 (0.14)I	−0.22 (0.14)I	−0.20 (0.15)I
Y	2.24	[Y II/Fe I]	−0.38 (0.07)I	−0.49 (0.10)I	−0.45 (0.08)I	−0.46 (0.07)I	−0.31 (0.08)I
Ba	2.13	[Ba II/Fe I]	+0.02 (0.08)I	+0.20 (0.10)I	+0.11 (0.08)I	+0.11 (0.08)I	+0.25 (0.09)I
Nd	1.50	[Nd II/Fe I]	+0.23 (0.09)I	+0.26 (0.12)I	+0.17 (0.10)I	+0.14 (0.10)I	+0.57 (0.11)I
La	1.22	[La II/Fe I]	+0.12 (0.08)I	−0.06 (0.10)I	+0.05 (0.08)I	+0.11 (0.09)I	+0.25 (0.09)I
Eu	0.51	[Eu II/Fe I]	+0.19 (0.13)I	+0.39 (0.17)I	+0.07 (0.14)I	+0.04 (0.14)I	+0.80 (0.15)I

NOTE.—See Table 7 notes.

them in quadrature over the entire range of stellar parameters. These *total internal uncertainties* are listed in Table 11.

In this paper plots of abundances will combine the statistical uncertainty and the internal uncertainties in quadrature to create a single error bar.

6.3. *External Errors*

External errors due to model atmospheres and analysis methods can be extremely difficult to diagnose and quantify. For example, using spectral indicators to determine the stellar parameters, rather than relying on the photometrically

TABLE 9
SCULPTOR ABUNDANCES

Elem.	Sun		Scl 459 AVG (Δ_r)	Scl 479 AVG (Δ_r)	Scl 461 AVG (Δ_r)	Scl 482 AVG (Δ_r)	Scl 400 AVG (Δ_r)
Fe	7.52	[Fe I/H]	−1.66 (0.02) 68	−1.77 (0.02) 67	−1.56 (0.02) 67	−1.24 (0.02) 67	−1.98 (0.03) 45
		[Fe II/H]	−1.65 (0.04)I	−1.79 (0.05)S	−1.58 (0.04)I	−1.26 (0.05)I	−1.94 (0.06)I
O	8.83	[OI/Fe I]	+0.22 (0.15)I	+0.48 (0.11)I	+0.44 (0.16)I	+0.18 (0.18)S	...
Na	6.33	[Na I/Fe I]	−0.33 (0.14)S	−0.59 (0.11)I	−0.55 (0.11)I	−0.55 (0.13)I	−0.16 (0.20)I
Mg	7.58	[Mg I/Fe I]	+0.36 (0.13)S	+0.26 (0.16)S	+0.18 (0.11)I	+0.09 (0.13)I	+0.37 (0.12)I
Al	6.47	[Al I/Fe I]	<+0.30	<+0.30	<+0.19	<−0.02	...
Si	7.55	[Si I/Fe I]	+0.22 (0.15)I	+0.00 (0.22)I	+0.14 (0.16)I	−0.07 (0.15)S	...
Ca	6.36	[Ca I/Fe I]	+0.24 (0.05)I	+0.17 (0.05)I	+0.22 (0.06)S	+0.06 (0.06)I	+0.38 (0.09)S
Sc	3.10	[Sc II/Fe I]	+0.01 (0.15)I	−0.05 (0.15)I	−0.22 (0.16)I	−0.38 (0.19)I	...
Ti	4.99	[Ti I/Fe I]	−0.05 (0.05)I	−0.05 (0.06)I	+0.00 (0.06)S	−0.17 (0.06)I	−0.07 (0.13)S
		[Ti II/Fe I]	−0.01 (0.08)I	+0.02 (0.09)S	−0.01 (0.08)I	−0.01 (0.10)I	+0.00 (0.09)I
Cr	5.67	[Cr I/Fe I]	−0.21 (0.11)I	−0.07 (0.11)I	−0.18 (0.11)I	−0.14 (0.13)I	−0.13 (0.14)I
Mn	5.39	[Mn I/Fe I]	−0.34 (0.08)I	−0.39 (0.09)S	−0.49 (0.08)I	−0.40 (0.09)I	...
Co	4.92	[Co I/Fe I]	+0.13 (0.15)I	+0.01 (0.11)I	+0.17 (0.16)I	−0.07 (0.19)I	...
Ni	6.25	[Ni I/Fe I]	+0.11 (0.12)S	−0.24 (0.09)I	+0.04 (0.09)I	−0.28 (0.11)I	+0.01 (0.20)I
Cu	4.21	[Cu I/Fe I]	−1.05 (0.15)I	−0.83 (0.15)I	−0.79 (0.11)I	−1.13 (0.19)I	< −0.46
Zn	4.60	[Zn I/Fe I]	+0.17 (0.15)I	−0.38 (0.15)I	−0.33 (0.15)I	+0.08 (0.19)I	...
Y	2.24	[Y II/Fe I]	−0.05 (0.12)S	−0.79 (0.08)I	−0.38 (0.09)I	−0.64 (0.11)I	+0.21 (0.23)S
Ba	2.13	[Ba II/Fe I]	+0.33 (0.09)I	−0.19 (0.09)I	+0.18 (0.09)I	+0.23 (0.11)I	+0.73 (0.17)S
Nd	1.50	[Nd II/Fe I]	+0.35 (0.11)I	−0.36 (0.11)I	+0.11 (0.11)I	−0.14 (0.19)S	+0.72 (0.20)S
La	1.22	[La II/Fe I]	−0.08 (0.09)I	−0.35 (0.15)E	−0.09 (0.12)E	+0.10 (0.19)I	+0.59 (0.13)S
Eu	0.51	[Eu II/Fe I]	+0.63 (0.15)I	+0.25 (0.15)I	+0.32 (0.16)I	+0.20 (0.19)I	+1.00 (0.20)I

NOTE.—See Table 7 notes.

TABLE 10
FORNAX AND LEO ABUNDANCES

Elem.	Sun		Fnx 12 AVG (Δ_r)	Fnx 25 AVG (Δ_r)	Fnx 21 AVG (Δ_r)	Leo 5 AVG (Δ_r)	Leo 2 AVG (Δ_r)
Fe	7.52	[Fe I/H]	−1.60 (0.02) 48	−1.21 (0.02) 64	−0.67 (0.03) 55	−1.52 (0.02) 67	−1.06 (0.02) 55
		[Fe II/H]	−1.59 (0.05)S	−1.17 (0.04)I	−0.73 (0.13)S	−1.48 (0.05)I	−1.10 (0.05)I
O	8.83	[O I/Fe I]	−0.02 (0.18)S	+0.17 (0.11)I	+0.12 (0.17)I	+0.53 (0.13)I	−0.04 (0.13)I
Na	6.33	[Na I/Fe I]	−0.51 (0.08)I	−0.31 (0.08)I	+0.02 (0.12)I	−0.43 (0.13)I	−0.36 (0.10)I
Mg	7.58	[Mg I/Fe I]	+0.09 (0.07)I	+0.02 (0.09)I	+0.20 (0.12)I	+0.12 (0.13)I	−0.19 (0.13)I
Al	6.47	[Al I/Fe I]	...	+0.09 (0.16)I	−0.04 (0.24)I	+0.42 (0.18)I	−0.28 (0.18)I
Si	7.55	[Si I/Fe I]	+0.29 (0.11)S	...	+0.08 (0.11)I	...	+0.00 (0.13)I
Ca	6.36	[Ca I/Fe I]	+0.23 (0.06)I	+0.21 (0.06)I	+0.23 (0.08)I	+0.15 (0.06)I	+0.02 (0.06)I
Sc	3.10	[Sc II/Fe I]	−0.11 (0.14)I	−0.16 (0.16)I	+0.05 (0.24)I	...	−0.81 (0.18)I
Ti	4.99	[Ti I/Fe I]	+0.03 (0.08)S	−0.14 (0.06)S	+0.38 (0.09)S	+0.11 (0.07)S	−0.06 (0.11)S
		[Ti II/Fe I]	−0.15 (0.08)S	−0.35 (0.09)I	+0.31 (0.24)S	+0.42 (0.13)S	+0.04 (0.12)S
Cr	5.67	[Cr I/Fe I]	−0.03 (0.13)S	+0.33 (0.16)I	−0.06 (0.32)S	+0.08 (0.14)S	...
Mn	5.39	[Mn I/Fe I]	−0.35 (0.10)I	−0.40 (0.08)I	−0.34 (0.15)S	−0.35 (0.09)I	−0.39 (0.10)I
Co	4.92	[Co I/Fe I]	+0.15 (0.29)S	+0.04 (0.15)S	+0.03 (0.23)S	...	−0.12 (0.13)S
Ni	6.25	[Ni I/Fe I]	−0.12 (0.16)I	−0.08 (0.09)I	−0.02 (0.12)I	−0.03 (0.09)I	−0.32 (0.09)I
Cu	4.21	[Cu I/Fe I]	−0.67 (0.14)I	−0.60 (0.16)I	+0.39 (0.24)I	−0.60 (0.13)I	−0.39 (0.13)I
Zn	4.60	[Zn I/Fe I]	−0.24 (0.14)I	+0.08 (0.16)I	...	−0.31 (0.18)I	...
Y	2.24	[Y II/Fe I]	−0.57 (0.09)S	−0.52 (0.14)I	+0.63 (0.22)S	−0.62 (0.13)S	−0.59 (0.09)I
Ba	2.13	[Ba II/Fe I]	−0.05 (0.08)I	+0.56 (0.11)I	+0.93 (0.14)I	+0.15 (0.11)S	+0.29 (0.13)S
Nd	1.50	[Nd II/Fe I]	+0.10 (0.10)I	+0.23 (0.11)I	+1.08 (0.18)S	+0.28 (0.18)I	+0.24 (0.13)I
La	1.22	[La II/Fe I]	−0.27 (0.08)I	−0.09 (0.13)S	+1.24 (0.17)S	+0.22 (0.17)S	+0.13 (0.16)S
Eu	0.51	[Eu II/Fe I]	+0.26 (0.14)I	+0.33 (0.16)I	+0.61 (0.24)I	+0.54 (0.18)I	+0.54 (0.18)I

NOTE.—See Table 7 notes.

derived parameters, can shift all of the $T_{\rm eff}$ and/or log g-values systematically up or down, which will affect the abundances. The magnitude of the effect on each element can be estimated from Table 6. As a demonstration, if the Alonso temperature scale had been adopted, then a shift in temperature by −60 K would have occurred, which shifts all of the [Fe I/H] abundances down by 0.06 dex. While this shift is small, it would also have occurred to the globular cluster standard star results. Since the interpretation of the abundances in the dSph galaxies depends on a differential comparison with the globular cluster standards, these small systematic shifts would not have a significant effect on the final results.

On the other hand, our comparison of MOOG/MARCS abundance results with those from ATLAS/WIDTH/VALD may be more valuable. As an example, the mean abundance results for the Sculptor star Scl 459 from each analysis method are shown in Table 12. As discussed above, the changes to the iron ionization equilibrium would force a slightly higher gravity in an ATLAS analysis. Small changes in gravity would have a negligible effect on the abundances from most of the neutral species, but a more significant effect on the derived abundances for O I and the ionized species. Thus, the absolute O/Fe ratio determined for an individual star could be affected (note that accurate O/Fe abundances is a problem with a large scope in metal-poor stars, and we refer to more specific papers on this problem, e.g., Lambert 2001; Asplund & Garcia Perez 2001). In this paper the interpretation of the O/Fe ratio is done with respect to standard stars whose analyses are done using the same techniques as the dSph stars. Thus, the *differential* O/Fe abundance ratios are similar whether derived from a MARCS/MOOG analysis or using the ATLAS/WIDTH techniques. The effect of changing the surface gravity on the ionized species is larger. While all of the *s*-process abundances could be affected by a significant amount (see Table 6, e.g., Ba II/Fe, Eu II/Fe), the comparison of Ba II/Y II or Ba II/Eu II will be far less affected. In addition, most of our comparisons of the ionized species abundances, such as [Ba II/Fe], should be similarly unaffected if the affect is systematic, since our comparisons will be made between our globular cluster giants and our dSph giants.

Other comparisons of abundance results in Table 12 show that the respective techniques do not produce and further discrepancies greater than 0.1 dex (the HFS of Mn and Cu were not included in the ATLAS/WIDTH analysis). It is also interesting to note that differences in the *gf*-values can still be important (causing >0.1 dex differences) in the analyses of Al, Sc, and Ti.

No corrections have been made to our abundances for non-LTE effects. We have attempted to compare our abundances with similiar LTE analyses to minimize this source of error.

7. GLOBULAR CLUSTER ABUNDANCES

Four red giants in three globular clusters were observed as standard stars to check our data reduction and analysis methods. There is excellent agreement in the metallicities derived in this paper with the iron abundances from Minniti et al. (1993), where δ[Fe/H] = −0.03 with σ = 0.16 dex, despite different line sets and oscillator strengths.

The globular cluster stellar abundance ratios are shown in Table 7. The abundances for these globular cluster stars are typical of those published for the halo (see McWilliam 1997) to within the statistical and internal errors, with the exception of Ti. Our Ti abundances fall about 0.15 dex below the typical Ti abundances (e.g., the Ti abundances from Fulbright 2002 who used the same line lists and very similar methodology). Reanalysis of the SCS01 dSph and

TABLE 11
ADOPTED INTERNAL ABUNDANCE UNCERTAINTIES

Elem.	σ_{dSph}	σ_{STND}
[O I/Fe I]	0.10	0.10
[Na I/Fe I]	0.05	0.05
[Mg I/Fe I]	0.05	0.05
[Al I/Fe I]	0.07	0.06
[Si I/Fe I]	0.08	0.05
[Ca I/Fe I]	0.02	0.02
[Sc II/Fe I]	0.07	0.07
[Ti I/Fe I]	0.07	0.07
[Ti II/Fe I]	0.08	0.08
[Cr I/Fe I]	0.05	0.05
[Mn I/Fe I]	0.07	0.07
[Fe I/H]	0.07	0.06
[Fe II/H]	0.11	0.08
[Co I/Fe I]	0.06	0.06
[Ni I/Fe I]	0.05	0.05
[Cu I/Fe I]	0.09	0.09
[Zn I/Fe I]	0.13	0.13
[Y II/Fe I]	0.06	0.06
[Ba II/Fe I]	0.08	0.08
[Nd II/Fe I]	0.06	0.06
[La II/Fe I]	0.14	0.16
[Eu II/Fe I]	0.09	0.08
[Y II/H]	0.15	0.10
[Ba II/Y II]	0.04	0.04
[Eu II/H]	0.05	0.05
[Ba II/Eu II]	0.10	0.09
[La II/Eu II]	0.04	0.04
[Nd II/Eu II]	0.08	0.07

NOTE.—The average internal errors are derived from a combination of the continuum uncertainties, metallicity uncertainties, and the stellar parameter uncertainties. The globular cluster standard stars often have smaller internal errors since the uncertainties in the continuum placement are significantly smaller.

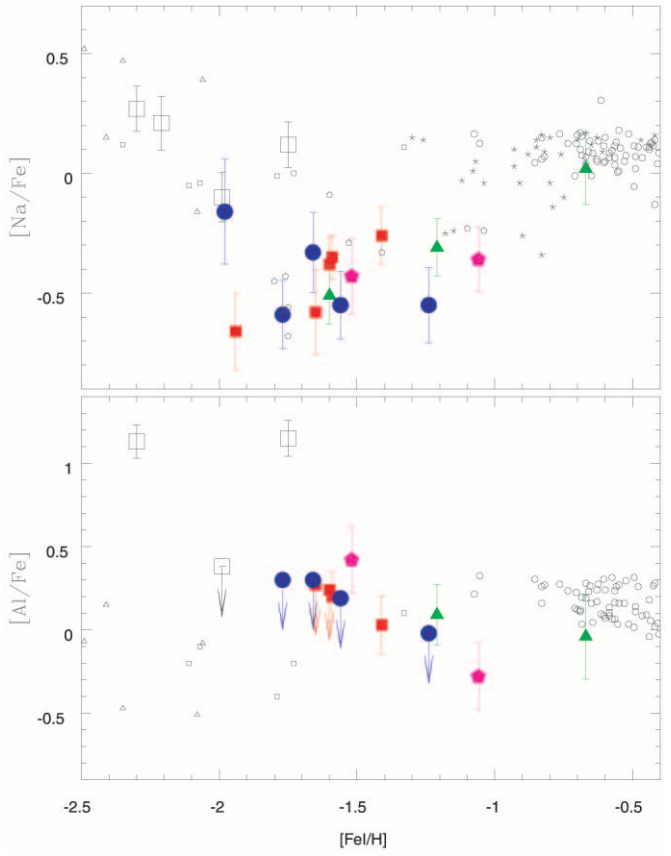

FIG. 2.—Na and Al abundances for our sample: Carina (*red squares*), Sculptor (*blue circles*), Fornax (*green triangles*), Leo I (*magenta pentagons*), and the globular cluster abundances (*large open squares*). The small symbols are taken from the literature to represent the disk, and halo populations: Edvardsson et al. 1993 (*small circles*), Nissen & Schuster 1997 (*small stars*), Stephens 1999 (*small pentagons*), Gratton & Sneden 1988 (*small squares*), and McWilliam et al. 1995 (*small triangles*). The error bars presented here are the systematic errors in Tables 7–10 and the internal errors from Table 11 added in quadrature.

globular cluster spectra, using only the lines adopted in this analysis, revealed only slightly smaller abundances (0.05 dex). Thus, we cannot account for this discrepancy and will limit our discussion of Ti in the dSph stars to differential abundances only.

We find that two, possibly three, of our four globular cluster standard stars show deep mixing. For metal-poor stars (with [Fe/H] = −2.0), deep mixing is detected as a star showing high [Al/Fe] and [Na/Fe] but low [O/Fe] and possibly low [Mg/Fe] (Shetrone 1996). In our sample, M30 D, M55 283, and M68 53 exhibit abundance ratios consistent with this pattern (see Fig. 2). Only M55 76 does not appear to have undergone deep mixing. For the Galactic field halo stars, the [O/Fe] and [Mg/Fe] abundances can be grouped with the other even-Z elements when there is no evidence of the deep mixing pattern.

8. DWARF SPHEROIDAL ABUNDANCES

In this paper we discuss the abundance pattern in the dwarf spheroidal stars by element and discuss the nucleosynthesis of these elements in comparison with the Galactic halo. A discussion of the element ratios by galaxy can be found in Paper II. Only Carina will be discussed separately here, which may show an α-element abundance pattern consistent with theoretical predictions for its bursting star formation history.

8.1. *No Deep Mixing in dSph Stars*

The surface abundances of Al and Na are very sensitive to deep mixing in red giants. Two (possibly three) of our globular cluster standards show elevated Al in Figure 2. In contrast, all of the dSph stars have halo-like Al/Fe ratios. One object in Leo I (Leo 5) may show a slightly elevated abundance ([Al I/Fe I] = +0.42), although this star shows a normal field halo-like Na and O abundances. In fact, all dSph stars show subsolar [Na/Fe] ratios. Thus, we do not expect any of the dSph stars have undergone deep mixing. As such we will include O and Mg in our discussion of the even-Z elements. The Na abundances in our study are consistant with the Stephens (1999) study of halo Na but fall below other studies, including our globular cluster sample, Gratton & Sneden 1988, and McWilliam 1995. The Stephens (1999) sample was selected to probe the outer halo and thus may be a slightly different sample than the other halo studies. This will be discussed in a later section.

TABLE 12
COMPARISONS BETWEEN MOOG/MARCS AND ATLAS/WIDTH FOR SCL 459

Elem.	MARCS/MOOG (this paper)	ATLAS/WIDTH	ATLAS/WIDTH and VALD *gf*-values
O I	7.39	7.32	7.39
Na I	4.34 (0.20)	4.42 (0.14)	4.46 (0.10)
Mg I	6.28 (0.20)	6.26 (0.08)	6.31 (0.02)
Al I	<5.11	<5.19	<4.96
Si I	6.11	6.18	6.18
Ca I	4.94 (0.15)	4.94 (0.10)	4.99 (0.11)
Sc II	1.45	1.42	1.53
Ti I	3.28 (0.12)	3.18 (0.27)	3.27 (0.23)
Ti II	3.32 (0.15)	3.23 (0.15)	3.40 (0.05)
V I	2.40 (0.51)	2.48 (0.35)	2.48 (0.33)
Cr I	3.80 (0.04)	3.78 (0.02)	3.78 (0.02)
Mn I	3.39 (0.08)	3.57 (0.08)	3.57 (0.08)
Fe I	5.86 (0.15)	5.98 (0.15)	5.97 (0.15)
Fe II	5.87 (0.15)	5.78 (0.18)	5.74 (0.15)
Co I	3.39	3.49	3.49
Ni I	4.70 (0.18)	4.75 (0.19)	4.78 (0.23)
Cu I	1.50 (0.15)	2.03 (0.09)	2.03 (0.08)
Zn I	3.11	3.05	3.02
Y II	0.53 (0.21)	0.47 (0.16)	0.47 (0.16)
Ba II	0.80 (0.15)	0.75 (0.13)	0.74 (0.13)
La II	−0.52 (0.09)	−0.52 (0.06)	−0.52 (0.03)
Nd II	0.19 (0.11)	0.16 (0.07)	0.20 (0.01)
Eu II	−0.52	−0.54	−0.54

8.2. *Even-Z Elements*

The theoretical picture for the formation of even-Z elements (O, Mg, Si, Ca, Ti) is in the nucleosynthetic shell-burning during SNe II at the end of the life of massive stars. This hypothesis is supported by elemental abundances in halo stars (see McWilliam 1997). It is also important to note that this theoretical picture generally applies to elements formed by α-capture, but the results from the halo stars suggest that Ca and Ti also follow this predicted behavior, and Ca and Ti are therefore lumped in with the α-elements. We will make a subtle distinction between the true (easy to understand) α-elements, O, Mg, and Si from the heavy even-Z elements Ca and Ti.

In the canonical picture of Galactic halo formation the even-Z elements are produced en masse shortly after a burst of star formation with so little time elapsing that SNe Ia have no time to dilute the pure SN II abundance pattern. At later epochs (>1.0 Gyr) SNe Ia had a chance to contribute. SNe Ia are thought to produce little to no O and Mg, while they probably are able to produce significant amounts of the iron peak even-Z elements Si, Ca, and Ti (see Woosley & Weaver 1995 and Table 3 in Iwamoto et al. 1999). Because of the under production of O and Mg by SNe Ia (Iwamoto et al. 1999), the [O/H] and [Mg/H] should remain constant and the [O/Fe] and [Mg/Fe] abundance ratios should decrease with increasing metallicity. Because SNe Ia produce some Si, Ca, and Ti, but less than are produced in SNe II, the [Si/H], [Ca/H], and [Ti/H] will rise slightly and the [Si/Fe], [Ca/Fe], and [Ti/Fe] will decrease slightly. In this scenario the even-Z elements slowly transition from a high value to a solar value with increasing metallicity (time).

The yields of the α abundances with respect to iron abundances in SNe II are mass dependent (Woosley & Weaver 1995) with higher masses producing a larger percentage of α-elements with respect to iron. If a small star formation event occurs, where relatively few high-mass stars are formed, then the most massive SNe II may not be present and the ratio of α-elements to iron could be altered from the canonical halo SN II abundance pattern. For example, with a Salpeter IMF (Salpeter 1955, and also see Massey2002 for the IMF for the Local Group) and a small 1000 $M_{\odot}$ star formation event, it is statistically unlikely that stars over 25 $M_{\odot}$ will form. Using the Woosley & Weaver 1995 SN yields, such an event will have much lower [O/Fe], [Mg/Fe], and [Si/Fe] abundance ratios (by 0.4 to 0.6 dex) with respect to a much more massive star formation event, where many higher mass stars are likely to form. This was also noted by Gibson (1998) in an examination of the upper limit to the IMF. *Thus, a low-mass star formation event could produce abundances that are slightly less enhanced than those found in the halo.*

As shown in Figures 3 through 8, even-Z abundance ratios are generally larger than solar in our metal-poor stars, as also seen in the halo. To produce these ratios requires reasonably massive early star formation events. The most metal-poor star in the Sculptor sample (H400) and the more metal-poor star in Leo I (Leo 5) have α-element ratios consistent with that of the halo (Gratton & Sneden 1988, 1991, 1994; McWilliam et al. 1995; Stephens 1999) indicating only a minor (if any) contribution from SNe Ia. In Sculptor (Figs. 4 and 7) and Leo I (Figs. 5 and 8), the even-Z–to–iron ratios appear to decrease as Fe increases. These trends are based on few data points and thus should be viewed carefully. To produce the decline in the even-Z abundance ratios requires either a later epoch of SN Ia contributions, or a later stage of small star formation events, which had

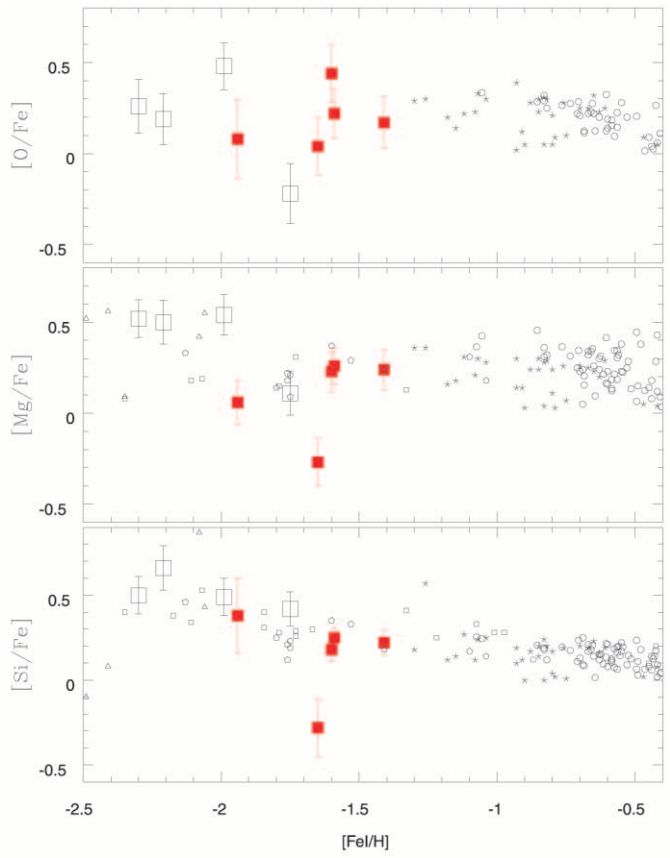

FIG. 3.—Carina [O/Fe], [Mg/Fe], and [Si/Fe] abundances (*red squares*) plotted against metallicity. The symbol types are the same as Fig. 2, with the addition of Gratton & Sneden 1991 and 1994 (*small squares*). The error bars presented here are the systematic errors in Tables 7–10 and the internal errors from Table 11 added in quadrature.

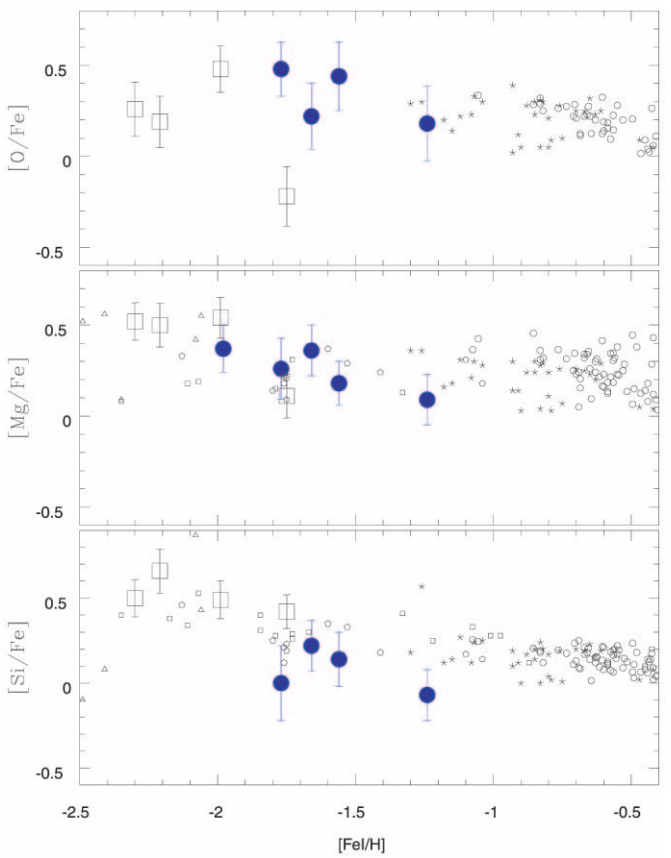

FIG. 4.—Sculptor [O/Fe], [Mg/Fe], and [Si/Fe] abundances (*blue circles*) plotted against metallicity. The symbol types are the same as Fig. 2. The error bars presented here are the systematic errors in Tables 7–10 and the internal errors from Table 11 added in quadrature.

fewer high-mass SNe II and thus produced lower even-Z abundance ratios.[3]

In Fornax (Figs. 5 and 8), the even-Z ratios appear flat to slightly rising. The average of the [O/Fe], [Mg/Fe], and [Si/Fe] abundance ratios is 0.1 dex ($\sigma = 0.1$), which is significantly smaller than that of the halo and our globular cluster sample (excluding the Mg and O for the stars with the deep mixing pattern). Again this can be done either through SN Ia contributions or from later smaller star formation events (lower mass SN II contributions). Fornax has a large spread in ages, as indicated from its color-magnitude diagram (see Mateo 1998; Paper II). Thus, one expects to have significant contribution from SNe Ia in the younger (more metal-rich) population.

The α-element abundance pattern in Carina (Figs. 3 and 6) exhibits a large and interesting dispersion, which we will address separately below.

8.3. *Iron Peak Elements*

The Cr, Co, and Ni abundances in the dSph stars are halo-like (Gratton & Sneden 1988, 1991, 1994; Sneden et al. 1991; McWilliam et al. 1995; Stephens 1999); i.e., they remain constant with Fe I to within the errors down to [Fe/H] ~ -2, as seen in Figure 9. Two stars near [Fe/H] ~ -1.1 (Leo I 2 and Scl H482) may also show slight Ni underabundance. This is interesting because Nissen & Shuster (1997) found a puzzling relationship between Ni and Na (and α-elements) in this same metallicity regime in halo stars; a tiny decrease in Ni is accompanied by a moderate decrease in Na (and α-elements) near [Fe/H] ~ -1. The Ni underabundance also seems to be related to lower α abundances (and possibly Na) in these two dwarf spheroidal stars.

Sc is also halo-like (i.e., flat near 0.0 dex) for most of our targets; however, a few stars (Leo 2, Car 3, and Scl 482) have significant underabundances. We also notice that the Sc abundances plotted in Figure 9 mimic the pattern of the α-elements better than that of the iron-group elements. Because the nucleosynthetic origin for Sc is unclear we will not comment further on Sc.

The Zn abundances in our dSph sample are systematically a few dex lower than those found in the Galactic halo (Sneden et al. 1991; Primas et al. 2000) and in our globular cluster sample. This seems to imply that the Zn is behaving differently from the other iron peak elements in *all* of these dSph. This is not entirely surprising since the nucleosynthetic origin of Zn is uncertain, with possible origins in SNe Ia, SNe II, and/or AGB stars (Matteucci et al. 1993; Hoffman et al. 1996; Umeda & Nomoto 2002).

8.4. Cu *and* Mn

The formation sites for Cu and Mn are not well known. In halo stars the Cu and Mn ratios are both less than solar

[3] For a review on the star formation histories of the Local Group galaxies, see Mateo 1998. A more detailed discussion of the star formation histories of our four dSph galaxies is included in Paper II.

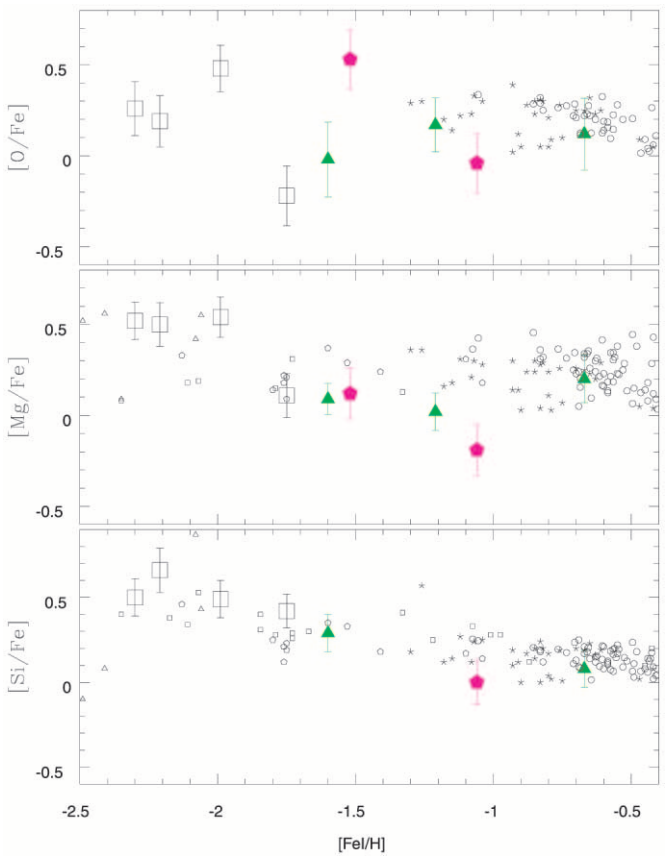

FIG. 5.—Fornax (*green triangles*) and Leo (*magenta pentagons*) [O/Fe], [Mg/Fe], and [Si/Fe] abundances plotted against metallicity. The symbol types are the same as Fig. 2. The error bars presented here are the systematic errors in Tables 7–10 and the internal errors from Table 11 added in quadrature.

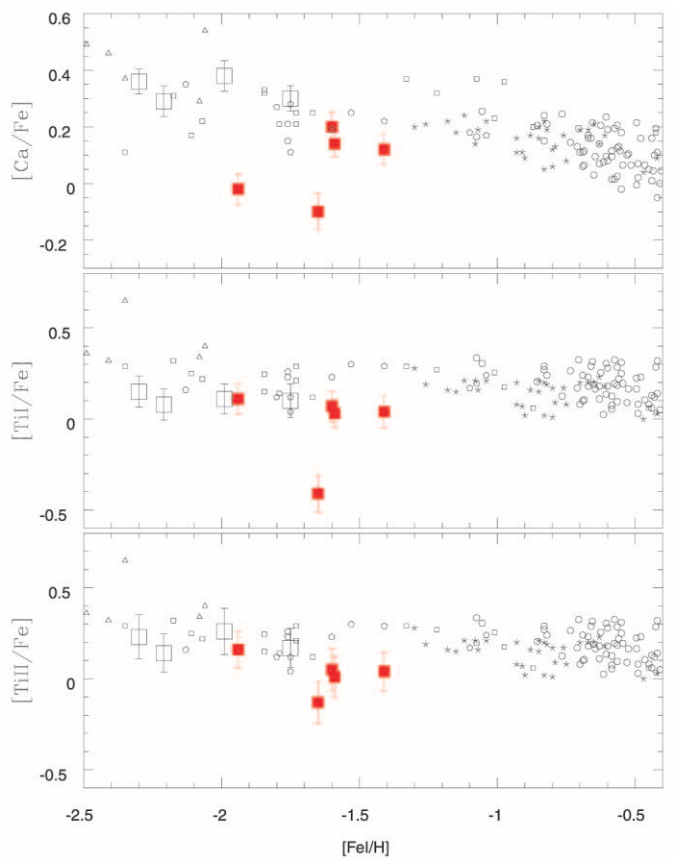

FIG. 6.—Carina (*red squares*) [Ca/Fe], [Ti I/Fe] and [Ti II/Fe] abundances plotted against metallicity. The symbol types are the same as Fig. 2. The error bars presented here are the systematic errors in Tables 7–10 and the internal errors from Table 11 added in quadrature.

until [Fe/H] ~ -1.0, when they both rise to solar (Gratton & Sneden 1988; Gratton 1989; Sneden et al. 1991; McWilliam et al. 1995). The most common interpretation of this pattern is that they are produced in SNe Ia (Gratton 1989; Matteucci et al. 1993; Samland 1998; Nakamura et al. 1999). Alternatively, Woosley & Weaver (1995) have suggested a metal-dependent SN II yield, such that, at [Fe/H] ~ -1, the metallicity becomes sufficiently high that significant amounts of Cu and Mn can be produced in the SN ejecta (see Timmes et al. 1995 for a chemical evolution model using the Woosley & Weaver 1995 yields).

As shown in Figure 10, our Cu and Mn ratios are consistent with the halo star abundances. They are less than solar over a wide range of low metallicities up to [Fe/H] ~ -1. The similar Cu, Mn, and Fe abundance patterns between the Galactic halo stars and the dSph stars suggest a similar abundance origin. In Figure 10 we also note that [Cu/α] is significantly less than solar and flat for the dSph stars (until [Fe/H] > -1). *This strongly suggests that either SNe Ia do not contribute to Cu in the most metal-poor stars, like the α-elements, or that any SN Ia contribution to Cu at this metallicity is not significant*. If significant amounts of Cu were being produced in metal-poor SN Ia events, then, as Fe increases, we would expect Cu/α to increase.

One may question, then, whether SN Ia products are contributing at all up to [Fe/H] $= -1$. As discussed in § 8, either SNe Ia are contributing, to explain the α/Fe ratios, or possibly only small star formation events have occurred (thus lower mass SNe II). However, also given the star formation histories for these galaxies as interpreted from their CMDs (see Paper II), it would be surprising if there were no SN Ia contributions until [Fe/H] $= -1$. All of these galaxies are thought to have had some star formation in the distant past (15 Gyr), with either continuous or bursting star formation at intermediate ages (5–10 Gyr). The intermediate-aged stars can be expected to form from gas enriched in SN Ia products from the earlier generation(s). Thus, we suggest that, if Cu is produced in SNe Ia, then the yield may be metallicity dependent, with increasing amounts of Cu as metallicity increases. It is also possible that the upturn in Cu/Fe near [Fe/H] $= -1$ is due to a metallicity-dependent SN II yield. This conclusion is not sensitive to the choice of HFS or *gf*-values because it is based on relative abundances within this analysis.

A similar argument can also be made for Mn. Figure 10 shows that Mn/Fe is also flat and halo-like. The halo stars appear to have increasing [Mn/Fe] above [Fe/H] $= -1$. In the halo the upturn has been intrepreted as the onset of SN Ia products. We suggest that, like Cu, SN Ia (or even SN II) contributions may be metallicity dependent, with very little Mn produced until [Fe/H] $= -1$.The system ω Cen is another one where [Cu/Fe] is quite low over the same range of ages and metallcities as our dSph stars (Cunha et al. 2002). Unlike the halo stars, [Cu/Fe] ~ -0.5 in the star in ω

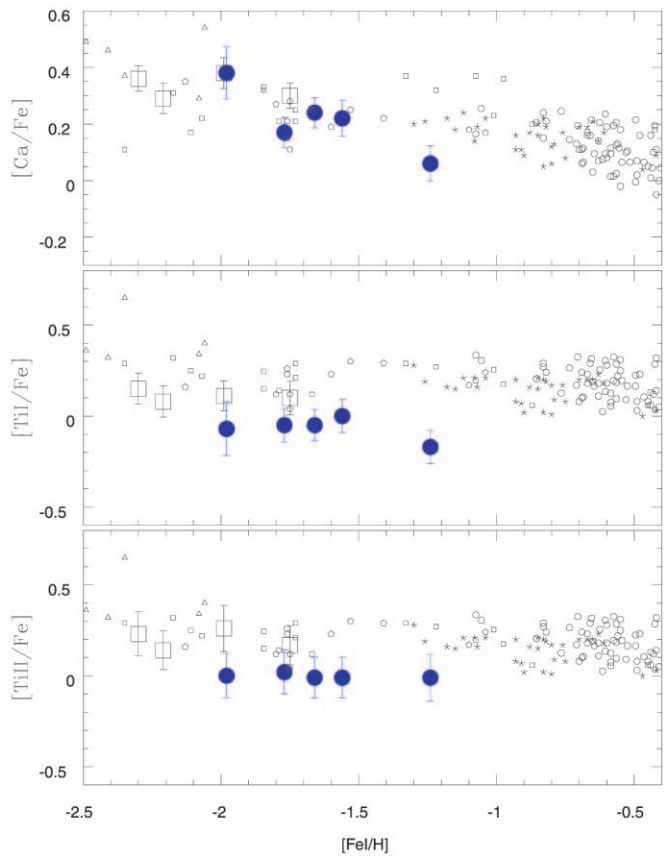

FIG. 7.—Sculptor (*blue circles*) [Ca/Fe], [Ti I/Fe], and [Ti II/Fe] abundances plotted against metallicity. The symbol types are the same as Fig. 2. The error bars presented here are the systematic errors in Tables 7–10 and the internal errors from Table 11 added in quadrature.

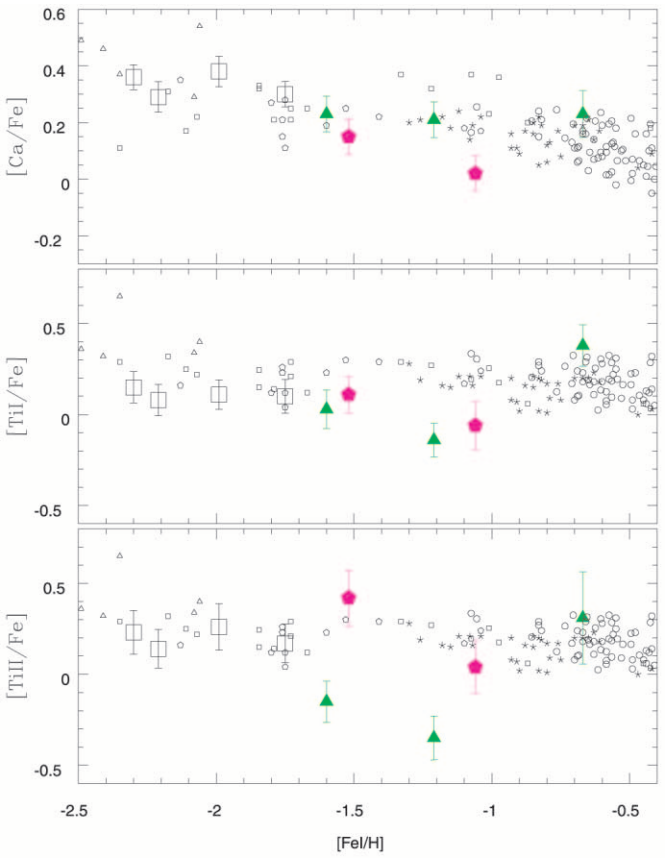

FIG. 8.—Fornax (*green triangles*) and Leo (*magenta pentagons*) [Ca/Fe], [Ti I/Fe], and [Ti II/Fe] abundances plotted against metallicity. The symbol types are the same as Fig. 2. The error bars presented here are the systematic errors in Tables 7–10 and the internal errors from Table 11 added in quadrature.

Cen and does not increase with metallicity. Our dSph results are not inconsistent with this result either, since our Cu/Fe ratios do not increase as quickly as in the halo stars. Cunha et al. similarly conclude that SNe Ia contribute very little to the chemical evolution of Cu in the metallicity range of $-2.0 < [Fe/H] < -0.8$. In contrast, Pancino et al. (2002) found an increasing [Cu/Fe] abundance with increasing metallicity for ω Cen giants in the metallicity range of $-1.2 < [Fe/H] < -0.5$. Both of these results could be interpreted as pollution from SNe Ia or as metal-dependent SN II yields. (A more detailed comparison of the abundance patterns observed in ω Cen with those found in the dSph is beyond the scope of this paper.)

8.5. *The First s-Process Peak Element,* Y

Y samples the first *s*-process peak, which may have a different source than the heavier (e.g., Ba) *s*-process elements. In Figure 11 we note that our most metal-poor stars have halo-like [Y/Fe] and [Ba/Y] ratios, implying a similar origin or different sources in the same proportion as were found in the halo (e.g., early SN II yields). But, as the metallicity increases, the [Y/Fe] abundance ratios decrease. This representation of the Y abundances is a bit misleading though. The central plot in Figure 11 shows the absolute Y abundances, [Y/H], where it can be seen that Y actually increases with metallicity for Carina, Leo I, and Fornax. The [Y/Fe] ratio decreases, though, because the Fe abundance is increasing more rapidly than the Y abundance is increasing in these dSph galaxies in comparison with the Galactic halo. For Sculptor, the [Y/H] abundance has a wide dispersion but remains constant over the metallicity range we sample.

A model for the formation of *s*-process elements in AGB stars by Clayton (1988) suggests that the yields scale with metallicity if the neutron source is the $^{13}C(\alpha, n)^{16}O$ reaction, and this model specifically predicts that [Ba/Y] should increase with metallicity. The bottom panel in Figure 11 shows that [Ba/Y] clearly does increase with metallicity in the dSph stars as predicted. That this pattern is not seen in the halo stars is more peculiar and suggests a number of possibilities. McWilliam (1997) discussed that the predicted [Ba/Y] relation in the halo may have been erased by the large metallicity dispersion in the halo; i.e., at any given time, the secondary elements are produced from stars with a variety of metallicities and thus yields. This interpretation predicts that the rising [Ba/Y] ratio in the dSph is caused by chemical evolution occurring over a longer period of time (in comparison with the halo), and thus AGB stars of a narrower range (in comparison to the halo) in metallcity are contributing to the ISM. Another option might be that that the seed for the first *s*-process peak (C?) is underabundant in the dSph galaxies. Low-resolution spectra of several dSph's show high carbon abundances, though, with respect to Galactic globular clusters of simi-

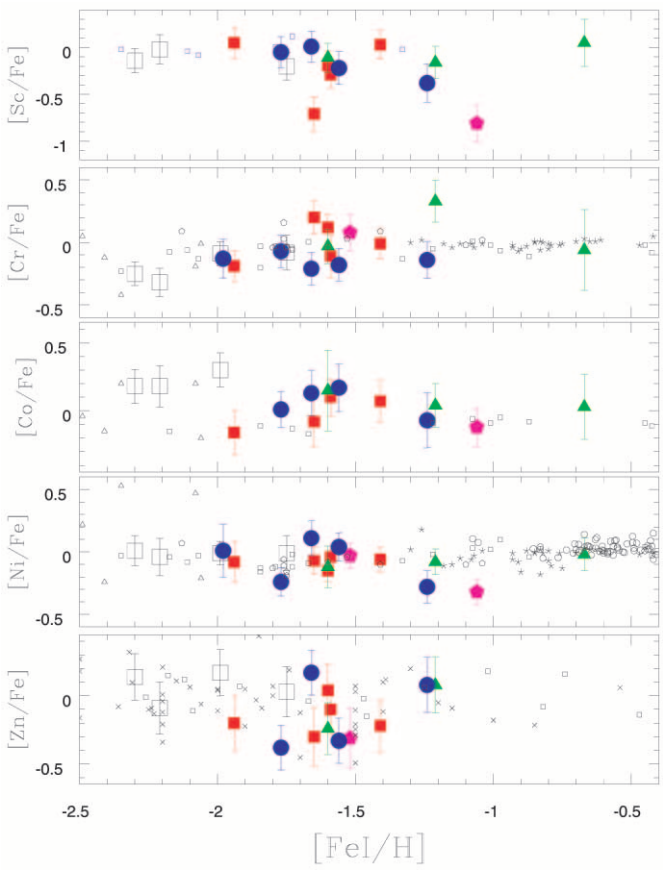

FIG. 9.—Iron peak abundances for our sample: Carina (*red squares*), Sculptor (*blue circles*), Fornax (*green triangles*), Leo I (*magenta pentagons*), and the globular cluster abundances (*large open squares*). The symbol types are the same as Fig. 2 with the addition of Sneden et al. 1991 (*small squares*) and Primas et al. 2000 (*crosses*). The error bars presented here are the systematic errors in Tables 7–10 and the internal errors from Table 11 added in quadrature.

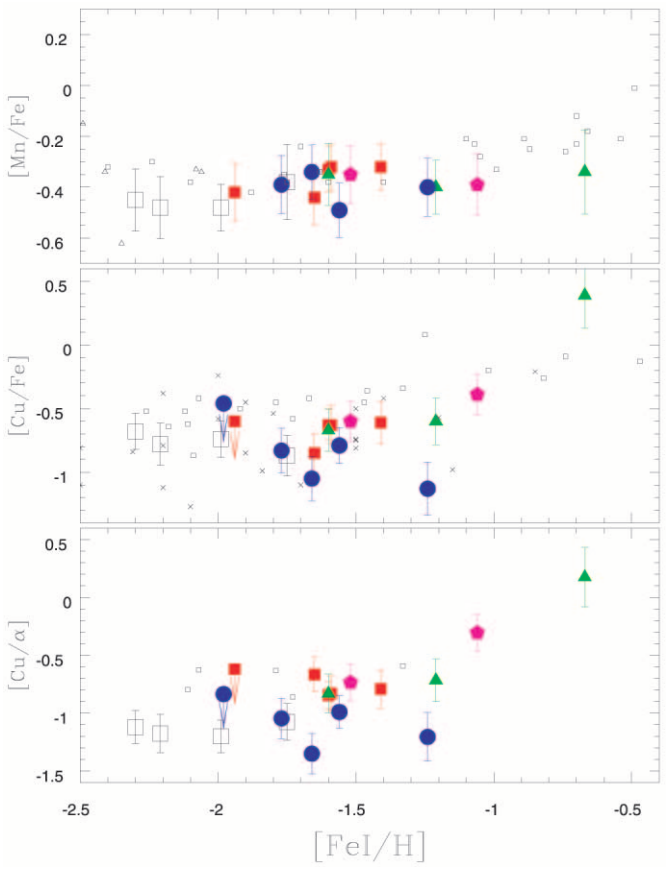

FIG. 10.—Mn and Cu abundances for our sample: Carina (*red squares*), Sculptor (*blue circles*), Fornax (*green triangles*), Leo I (*magenta pentagons*), and the globular cluster abundances (*large open squares*). The small symbols are taken from the literature to represent the disk, and halo populations: Gratton 1989 (*small squares*), McWilliam et al. 1995 (*small triangles*), Gratton & Sneden 1988 (*small squares*), Sneden et al. 1991 (*small squares*) and Primas et al. 2000 (*crosses*). α is defined as the average of the Mg and Ca abundances. The error bars presented here are the systematic errors in Tables 7–10 and the internal errors from Table 11 added in quadrature.

lar metallicities (Kinman et al. 1980; Smith & Dopita 1983; Smith 1984; Bell 1985). A third option, if we forgo Clayton's model, could be that there is a source of Y in the Galactic halo that is not present in the higher metallicity dSph stars. Since most studies of SN II yields do not include the first *s*-process peak, we cannot compare this hypothesis with any models. The first option is the most consistent with the overall abundance patterns.

The Y enrichment in the metal-rich Fornax star, Fnx 21, is consistent with other *s*-process enrichments in this star (discussed below).

8.6. *s-Process and r-Process Elements*

In the Sun Eu is largely an *r*-process element (95%, Burris et al. 2000). The site of the *r*-process has been suggested to be low-mass SNe II (Mathews, Bazan, & Cowan 1992), but the site for the *r*-process is still a matter of debate (e.g., Wallerstein et al. 1997; Tsujimoto & Shigeyama 2001; Qian 2002). However, most of these models share a common prediction: SNe II are the source of the *r*-process. Thus, [Eu/H] should rise whenever SNe II contribute to the ISM, and only when SNe Ia and AGB stars contribute to the ISM should [Eu/H] remain constant and the [Eu/Fe] ratio decline. The Eu abundances are plotted in Figure 12. In Leo I and Fornax the [Eu/H] abundance increases with metallicity as expected, if there has been some ongoing star formation with SNe II contributing to the ISM. A similar slope is also seen in the Galactic halo stars (Gratton & Sneden 1991, 1994; McWilliam et al. 1995; Burris et al. 2000). Thus, we predict a burst of star formation between [Fe/H] = −1.5 to −1.1 for Leo I and −1.5 to −1.2 for Fornax. These predictions are provisional, given the few number of points and the large error bars. On the other hand, the Sculptor [Eu/H] abundances are relatively flat over the entire metallicity range sampled, which implies little to no later contribution of SNe II to the ISM. Thus, for Sculptor we predict that only a single burst occurred or that the material from SNe II was completely lost from the galaxy in any later bursts. The Carina abundances will be discussed separately below.

Oddly, the most metal-poor star in Sculptor, H-400, has a larger [Eu/H] abundance than Galactic halo stars of similar metallicity. The top panel of Figure 12 shows that this star has [Eu/Fe] = +1.0, and, as we will show later, an *r*-process–dominated abundance pattern. This type of super *r*-process–rich abundance pattern has been seen among Galactic halo stars (McWilliam et al. 1995) and attributed

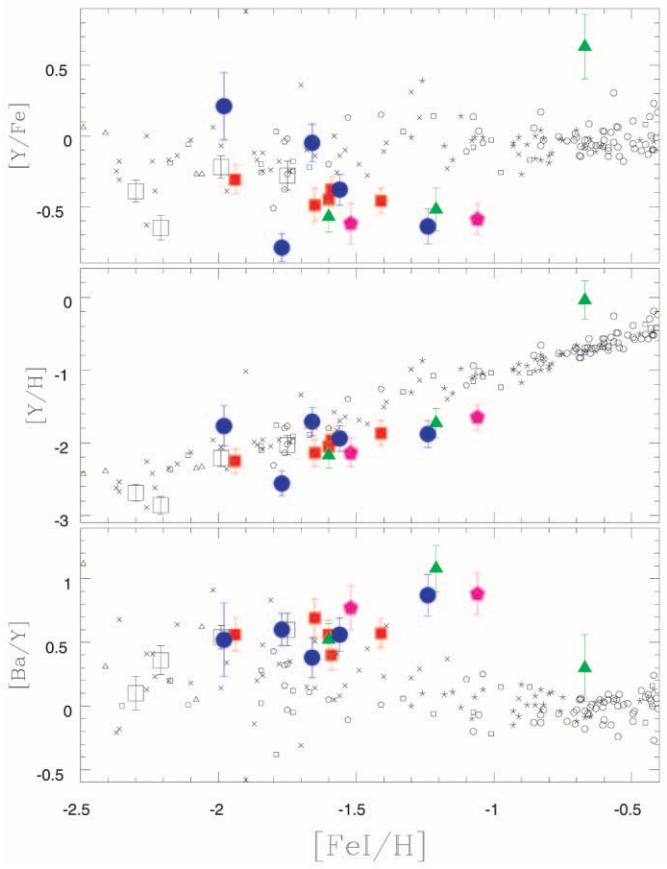

FIG. 11.—Y and Ba abundances for our sample: Carina (*red squares*), Sculptor (*blue circles*), Fornax (*green triangles*), Leo I (*magenta pentagons*), and the globular cluster abundances (*large open squares*). The small symbol types are the same as Fig. 10 with the substitution of Burris et al. 2000 (*small crosses*). The error bars presented here are the systematic errors in Tables 7–10 and the internal errors from Table 11 added in quadrature.

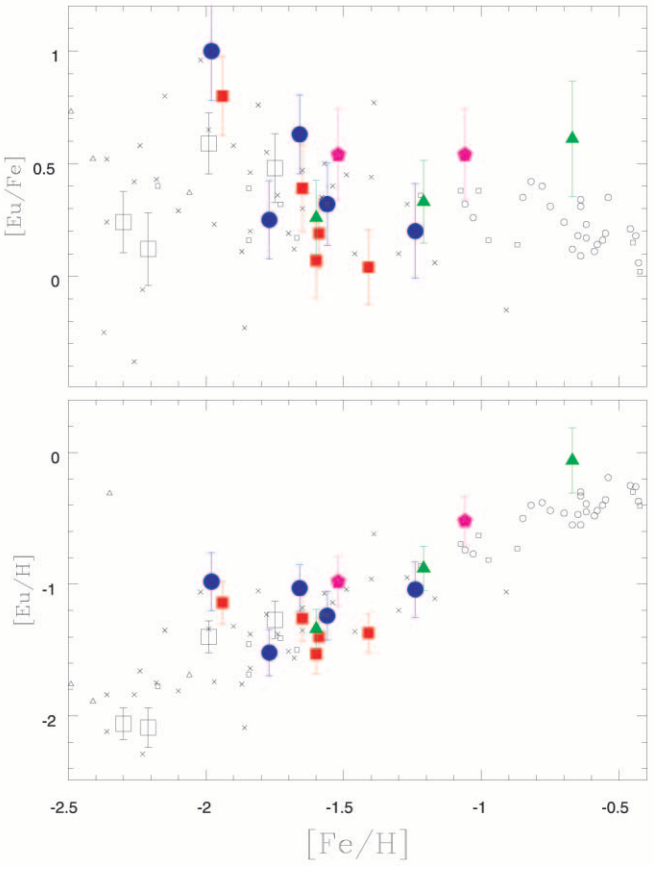

FIG. 12.—The Eu abundances for our sample: Carina (*red squares*), Sculptor (*blue circles*), Fornax (*green triangles*), Leo I (*magenta pentagons*), and the globular cluster abundances (*large open squares*). The small symbol types are the same as Fig. 9, with the addition of Eu for the Edvardsson et al. 1993 coming from Koch & Edvardsson 2002 and the small crosses representing data from Burris et al. 2000. The error bars presented here are the systematic errors in Tables 7–10 and the internal errors from Table 11 added in quadrature.

to inhomogenous mixing of the SN II yields (McWilliam et al. 1997); i.e., the star forms after the local ISM is contaminated by a nearby *r*-process–rich SN II and before the ISM is well mixed. However, all of these Galactic *r*-process–rich stars are more metal-poor than H-400. This high [Eu/Fe] abundance could be due to a wide dispersion in [Eu/H] at [Fe/H] = −2.0, and we have only sampled the upper end of that distribution.

A comparison of *s*- and *r*-process elements with Eu (a largely *r*-process element) allows us to examine the contributions to the abundances from AGB stars. The *s*-process/*r*-process ratios are shown in Figure 13. The pure *r*-process contributions to these elements from Burris et al. (2000) are shown by the dotted lines, while the solid line shows the pure *r*-process contributions from Arlandini et al. (1999). The Burris et al. contributions are calculated using the "classical approach," which models the neutron flux of an AGB star with a simple analytical model. The Arlandini et al. values come from a new generation of AGB evolutionary models. Of course, comparison with these solar-system fractions requires our abundances to be on an absolute scale and introduces many additional concerns. The *r*-process fractions should be considered free parameters, able to slide up or down within our abundance scale. It is important to stress that La and Ba are often called *s*-process elements based on the fraction of these elements that were produced by the *s*-process *in the Sun*. However, in the early universe and apparently in the most metal-poor stars in these dSph's we expect that all the heavy elements present have their origins in the *r*-process, since AGB stars would not have had time to evolve and contribute to the ISM (Truran 1981). Indeed, in our most metal-poor stars the Ba, Nd, and La abundances are consistent with primarily *r*-process contributions. Note that, in the Sun, La and Ba are mostly *s*-process elements (85% and 75%, respectively, from Burris et al. 2000, while Nd is thought to be [roughly] half produced in the *s*-process and half in the *r*-process. Nd alone does not actually constrain the abundance contributions significantly.

The [Ba/Eu] and [La/Eu] ratios in Sculptor, Fornax, and Carina clearly increase with metallicity, as in the halo stars. This suggests that some level of star formation must have continued after any initial, early-epoch star burst, so that subsequently more metal-rich objects could be contaminated from the early metal-poor AGB stars. Of course, this contamination timescale must be *greater* than the life time of the AGB stars (∼1 Gyr). The seemingly flat [Ba/Eu] and [La/Eu] ratios in Leo I suggest that the contribution from AGB stars must have been fairly small (from metallicity [Fe/H] = −1.5 to [Fe/H] = −1.1). Thus, the timescales

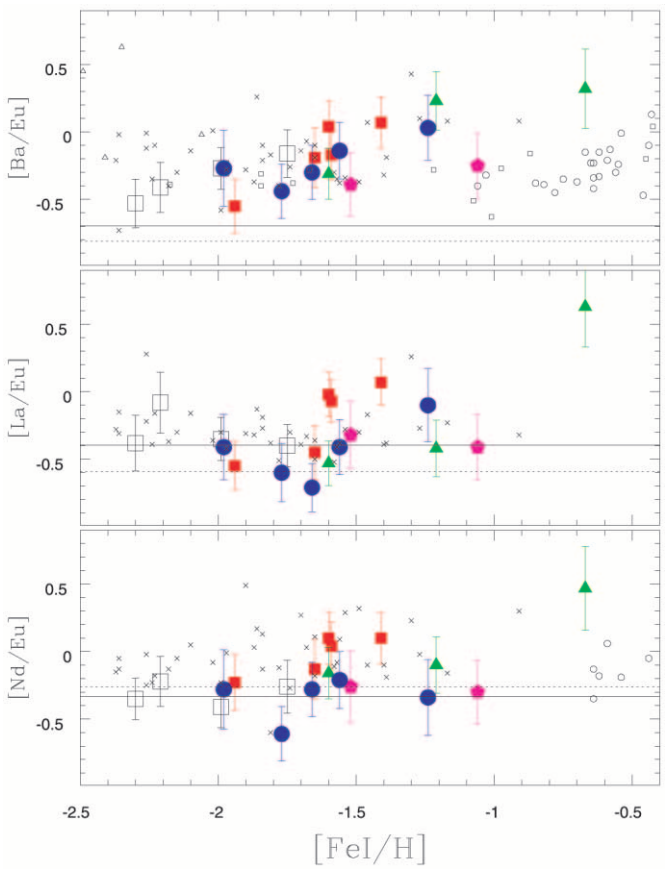

FIG. 13.—The *s*- and *r*-process element ratios for our sample: Carina (*red squares*), Sculptor (*blue circles*), Fornax (*green triangles*), Leo I (*magenta pentagons*), and the globular cluster abundances (*large open squares*). The small symbol types are the same as Fig. 10, with the addition of Eu for the Edvardsson et al. (1993) sample coming from Koch & Edvardsson 2002 and the small crosses representing data from Burris et al. 2000. The dotted line represents the pure *r*-process abundance ratios from Burris et al. 2000. The solid line represents the pure *r*-process abundance ratios from Arlandini et al. 1999. The error bars presented here are the systematic errors in Tables 7–10 and the internal errors from Table 11 added in quadrature.

between these two epochs should have been fairly short. A short timescale between these two epochs would imply that there should be little SN Ia contribution during this period, and thus any decline in the even-Z elements would be due to small star formation events and thus few high-mass SNe II to produce α-elements. More stellar abundances in this metallicity range would help to confirm this suggestion, since, with only two stars, we cannot rule out a small slope in the [Ba/Eu] and [La/Eu] ratios.

The metal-rich star in Fornax, Fnx 21, shows remarkable enrichment in all *s*-process elements (and possibly Eu), often greater than the enrichments in the Galactic halo stars, and clearly shows a supersolar s/r ratio. The most likely possibility is that this star underwent mass transfer in a binary system with an evolved AGB star. However, with such a small sample of stars, we cannot rule out the possibility that the most metal-rich stars in Fornax have had a very large *s*-process enrichment from AGB stars in comparison with the total number of *r*-process SN events. However, this second hypothesis seems to contradict the slightly enhanced α/Fe ratio and an increasing [Eu/H] abundance with increasing metallicity, which imply the continued contribution from SNe II. Only analyses of additional metal-rich stars in Fornax will be able to distinguish between these two possibilities.

8.7. *Carina's Abundance Pattern*

Carina has a bursting star formation history as determined from its CMD (Hernandez, Gilmore, & Valls-Gabaud 2000; Hurley-Keller et al. 1998; Smecker-Hane et al. 1994; Mighell 1990). One might expect to see this signature in the α-element/Fe ratios. After *each* burst, the α-element ratio increases rapidly (because of the rapid influx of α-rich SN II material; e.g., Gilmore & Wyse 1991), followed by a slow decline as Fe is produced by the SNe Ia. Of course, to sample this pattern would require some low level of star formation between each burst. Also, this assumes a fully sampled IMF, which may not occur (statistically) in very low mass star formation events.

In Carina we may see this pattern for the first time in any Galactic system.[4] Our most metal-poor star (Car 10, [Fe/H] $= -1.94$) has slightly enhanced [α/Fe] ratio, but the next most metal-poor star (Car 3, [Fe/H] $= -1.65$) has quite a low [α/Fe]. In addition the [α/H] ratio of Car 10 and Car 3 are nearly the same, which implies that the increase in iron peak elements was not accompanied by any detectable increase in the α-elements, as is expected from SNe Ia. The remaining three objects return to high [α/Fe] (perhaps even higher than Car 10), as predicted if a burst of star formation followed that polluted the interstellar medium with α-elements. If this interpretation is correct, the burst must have happened between [Fe/H] $= -1.65$ and [Fe/H] $= -1.60$, according to our iron abundances; this is the metallicity range predicted $\sim$7 Gyr ago, when a burst lasting 2–4 Gyr is predicted by Hurley-Keller et al. (1998) and Hernadez et al. (2000). Further discussions of ages and burst populations are discussed in Paper II.

The pattern repeats in all of the α-elements, strongly suggesting that this is not a problem with a particular set of absorption lines (e.g., that Car 3 and its analysis is *not* unusual). We also strongly suggest that this is not a pattern brought on by atmospheric parameter uncertainties, since the Fe abundances and temperatures are quite typical. The only distinction is that Car 3 has a very low gravity determination; however, most of the α-element ratios are *not* sensitive to gravity (e.g., Mg, Si, Ca, Ti; see Table 6), and they still show this pattern.

In addition to the α-abundance pattern in the five Carina stars we find supportive evidence that their chemical abundances are related to the star formation history in the *s*- and *r*-process ratios as well. The Ba, La, Nd, and Eu abundances are to be found primarily *r*-process abundance pattern in the most metal-poor star (Car 10, [Fe/H] $= -1.94$). In the next star (Car 3, [Fe/H] $= -1.65$) the Ba/Eu, La/Eu, and Nd/Eu appear to be very slightly larger, suggestive of some small *s*-process enrichment; the SFH by Hurley-Keller et al. 1998 suggests a 3 Gyr hiatus between the first and second bursts of star formation, which is sufficient time for AGB stars to contribute some *s*-process fraction. The next two stars, with [Fe/H] $= -1.6$, show a significant increase in

[4] Very recent analyses of red giants in LMC clusters may also show the α/Fe ratios predicted from bursting star formation history models (Hill 2003).

La/Eu and also slight increases in Ba/Eu and Nd/Eu. This suggests further AGB contributions. The increase in their α-elements implies SN II contributions, which could also provide the *r*-process elements and drive down the ratio of *s*-process to *r*-process abundances, but we do not see this. Possibly, very little *r*-process elements were formed or were incorporated into the ISM when these stars formed, or the AGB contributions were simply more significant. It is important to point out that we are not predicting that Car 3 was formed in the second burst. Car 3 could have been formed in an intermediate star formation event some considerable time before the second burst and thus further AGB contamination could have occurred.

One difficulty in the interpretation of the chemical evolution of Carina as a burst pattern is the flat (or even declining) [Eu/H] abundances, see Figure 12. If we expect significant SNe II between the Car 3 and the [Fe/H] = −1.6 Carina stars, then we might expect a rise in the [Eu/H] abundance, since Eu (as a primarily *r*-process element) is thought to be produced in SNe II. One possible explanation for this contradiction is that the mass range of SNe that produce most of the Eu at this metallicity is narrow enough that a low-mass IMF would restrict the number of these events. Another possibility is that some of the subsequent *r*-process material has been lost from the galaxy (blowout?). Since we detect a factor of 2 increase in the even-*Z* abundance, the blowout would have to be very selective. But a final possibility is simply that we have underestimated our errors for the Eu abundance based on this single very weak line and cannot detect a subtle increase in Eu that may be present.

Figure 14 is an alternative way to view the entire chemical evolutionary history for Carina. Figure 14 shows the abundance pattern for Car 10, Car 12, and Car 3. The abundance pattern has been normalized to Mg for the light elements and normalized to Eu for the heavy elements. The top panel shows the solar-system abundance pattern as a solid line, and the dotted line represents the abundance pattern implied by SNe II-L) from Qian & Wasserburg (2002), while the dashed line represents the the *r*-process abundance pattern from Arlandini et al. (1999). The solid line and the dotted line deviate furthest apart in the iron peak, elements Cr–Ni. We show the abundance pattern of three Carina stars, with filled squares representing Car 10 (our most metal-poor Carina giant), crosses Car 3 (the Carina giant with the extremely low α-to-iron abundance ratio), and open squares Car 12 (our most metal-rich Carina giant). Among the iron peak elements the Car 3 abundances stand out as anomalous, while the Car 12 and Car 10 abundances lay between the solar and SNe II-L abundance patterns. Among the heavy elements there appears to be a spread in the abundance pattern, with Car 10 fitting the Arlandini et al. (1999) pure *r*-process abundance pattern and Car 12 being closest to a solar abundance pattern. Because of the large dynamic range in the top panel of Figure 14 a comparison between the different abundance patterns is difficult.

The bottom panel for Figure 14 shows the same abundance pattern, but with the average globular cluster abundance removed. Since we only have a single globular cluster star without the deep mixing abundance pattern, we have adopted the Mg and O abundances from that star (M55 76) and have excluded Na and Al. The points in the bottom panel of Figure 14 are the same as those given in the top, with the addition of open circles, which represent the solar abundance pattern. The elements below atomic number 20 (i.e., O, Mg, Si) are similar to those of the globular cluster, but the iron peak elements (i.e., atomic number 21–30) are clearly overabundant. The times crosses (Car 3) exhibit the highest overabundance in the iron peak. As mentioned before, we interpret this to be a due to a long period of SN Ia contamination before a later burst, which brings the peak back down (or the α-elements back up). The fact that the most metal-poor Carina star (Car 10) shows an overabundance of iron peak elements does not necessarily mean that SNe Ia have contributed to its abundance pattern, since, as we have mentioned previously, a low-mass star formation event can produce a low α abundance pattern with respect to the iron peak. The heavy elements also show a clear evolution toward the solar abundance distribution (the open symbol Car 12 is the most metal-rich in the Car sample and shows the most solar-like heavy element abundance distribution). We interpret this to mean that significant time has passed between the formation of each of these dSph stars, i.e., to allow subsequent AGB contamination.

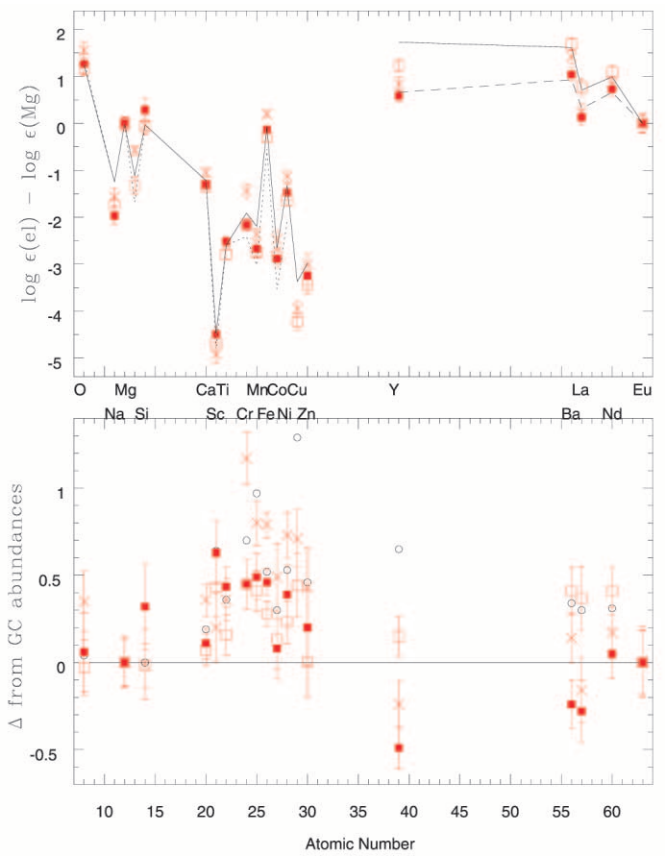

FIG. 14.—*Top*: Abundance patterns for Car 10 (*red filled squares*), Car 12 (*red open squares*), and Car3 (*red crosses*) normalized to the Mg abundance, for the light elements and Eu for the heavy elements. The solid line is solar abundance pattern, the dotted line is the predicted SN II-L abundance pattern from Qian & Wasserburg (2002), and the dashed line is the pure1 *r*-process abundance pattern from Arlandini et al. (1999). *Bottom*: Residual abundances pattern for the same three stars after subtracting off our observed globular cluster abundance pattern. The open circles represent the solar-system abundances. The Na and Al abundances are excluded in the bottom panel. The error bars presented here are the systematic errors in Tables 7–10 and the internal errors from Table 11 added in quadrature.

If this burst-like abundance pattern can be supported with other stars in Carina in this metallicity range (near [Fe/H] = −1.6), then this would be the first proof of the theoretical bursting-galaxy chemical-enrichment models.

9. DISCUSSION

The underabundance of the α-elements (with respect to globular cluster stars) found at [Fe/H] = −1.5 can be interpreted in two ways: either as the onset of SNe Ia at lower metallcities than is found in the halo or as a small star formation event where there are very few massive stars (the ones that produce the α-elements). Since the IMF is similar in nearly every environment in which it is studied (e.g., Magellanic Clouds and Galactic clusters, Massey 2002), then usually the α-element ratios are interpreted in terms of the onset of SNe Ia, but the effect of the absence of many massive stars in a small star formation event should not be ignored. However, for Fornax and Carina, where a large spread in ages is expected (see Mateo 1998; Hernandez et al. 2000; Hurley-Keller et al. 1998; Smecker-Hane et al. 1994; Mighell 1990; and Paper II), SN Ia contamination should be expected at higher metallicities.

We also note that, if the iron peak enhancements (as seen in Fig. 14) are due to SNe Ia, over the metallicity range $-2 <$ [Fe/H] < -1, and yet the [Mn/Fe] and [Cu/Fe] remain flat, then SNe Ia cannot be the cause of the upturn in Mn and Cu seen among the Galactic halo stars. This is also supported by the very low [Cu/α] ratios shown in Figure 10. As discussed in § 8.4, we suggest that a metallicity-dependent SN yield (e.g., SN II, Timmes et al. 1995) may be the formation site for Cu and Mn in metal-poor stars.

A similar type of argument can also be made for the source of the first *s*-process peak in metal-poor stars. Since the timescales for SN Ia and AGB contamination are similar, and the slopes of [Y/H] versus [Fe/H] are different between the Galactic halo stars and the dSph stars, then the source for Y in metal-poor stars is neither SNe Ia nor AGB stars. *It must come from another source, such as SNe II (again possibly a metallicity dependence).* The large [Ba/Y] ratio seen in the dSph stars with [Fe/H] > -1.6 (see Fig. 13) might be due to Ba (but not Y) being enhanced by the *s*-process. The fact that the most metal-rich star in Fornax, Fnx 21, has Ba/Y that is halo-like is a result of increased Y (also seen in Fig. 13), mostly likely because Y has been enhanced by a greater factor than Ba (since Ba and La are also enhanced in this star) from more metal-rich AGB stars. If Zn also has a small component that is linked to the first *s*-process elements, then the slight underabundance of Zn might be linked to the underabundance of Y.

9.1. *DSph Abundances and the Galactic Halo*

Several lines of evidence suggest that the Galactic halo is composed, at least partially, of accreted dSph galaxies. These include the current assimilation of the Sgr dwarf (Ibata et al. 1997; Dohm-Palmer et al. 2000; Newberg et al. 2002) and possibly ω Cen (Majewski et al. 2000, assuming that it is a stripped dSph). The abundances presented here for the metal-poor stars in four dSph's show a strong iron peak signature (regardless of the origin) or viewed differently as low α-to-iron ratio with respect to Galactic halo stars. Since the halo's metallicity distribution peaks near [Fe/H] = −1.8 and those stars show a higher α-to-iron ratio than the dSph stars (see Figs. 3–8 in this work and Fig. 12 in Fulbright 2002), clearly a large percentage of the halo cannot have been produced from dSph's similar to those analyzed here, or we would see a many stars with a strong iron peak abundance pattern in the halo. Fulbright (2002) found that less than 10% of the local metal-poor ([Fe/H] < -1.2) stars have α-to-iron abundance ratios similar to those found in the dSph sampled in this work and SCS01. However, by subdividing his sample by total space velocity, the highest space velocity stars have systematically lower α-to-iron abundance ratios. Stephens's (1999) sample was kinematically selected to probe the outer halo by looking for high-velocity local stars. This sample also exhibits low [Na/Fe] ratios and low even-*Z*–to–iron ratios (with respect to the other halo samples). At the same metallicities as the Stephens (1999) sample, our dSph samples have low [Na/Fe] and even lower even-*Z*–to–iron ratios. Perhaps the disrupted dSph's similar to those studied in this work contribute to the the high space velocity tail of the Galactic halo.

Nissen & Schuster (1997) conducted a detailed abundance analysis of a nearby sample of disk and halo stars with similar metallicities to study the disk-halo transition. Their sample was chosen to get an equal number of disk and halo stars as defined by the stars stellar rotation. Of their 13 chosen halo stars, eight show an unusual abundance pattern: low α-element–to–iron ratio, low [Ni/Fe] abundances, and low [Na/Fe] abundances. These odd halo stars also exhibited larger $R_{\max}$ and $z_{\max}$ orbital parameters than the other halo stars sampled. Nissen & Schuster (1997) suggest that these anomalous stars may have their origins in disrupted dSph's. The dSph stars in our sample at a similar metallicity [Fe/H] = −1.0 also exhibit subsolar [Na/Fe] and [Ni/Fe] and low even-*Z*–to–iron abundances. This seems to lend support to the idea put forward by Nissen & Schuster (1997), that a large fraction (>50%) of the metal-rich halo may have their origin in disrupted dSph's like those studied in this work.

This still leaves the question of the origin of the metal-poor halo, though, and the fraction of the metal-poor halo that formed through monolithic collapse versus accretion of dSph galaxies. We note that we have examined the [α/Fe] ratios in a subset of the dSph stars, that is, those with the oldest ages (∼15 Gyr, from Paper II). On average, [α/Fe] ∼ +0.15, with a range from solar to +0.4. This average is still lower than the metal-poor (presumably old) halo stars, yet the range does overlap. It is likely that some fraction of the old, metal-poor halo is composed of disrupted dSph's like those examined here, but we continue to agree with SCS01, that the dSphs cannot account for the majority.

9.2. *Connection to other dSph Galaxies*

There are not a large number of publications with high-resolution, detailed abundance analyses of dSph stars. Bonifacio et al. (2000) and Smecker-Hane & McMilliam (2002) have samples of stars in the Sagittarius dSph. Shetrone et al. (1998) analyzed four giants in the Draco dSph, and these results were incorporated into SCS01 to yield a sample of six giants in Draco, six giants in Ursa Minor, and five giants in Sextans.

The SCS01 sample should be the most straight forward to compare with this work, since many of the methods are the same. The population sampled in Draco, Ursa Minor, and Sextans contains more very metal-poor ([Fe/H] < -2)

stars, so we shall restrict ourselves to comparisons between $-2 < [Fe/H] < -1$. The overall abundance distribution differences could be better addressed in a low-resolution abundance population paper. In this restricted metallicity range the Draco, Ursa Minor, and Sextans samples have very similar abundance patterns to the dSph abundance patterns of Sculptor, Fornax, Leo I, and Carina. This includes underabundant α-to-iron abundance ratios with respect to the halo, a slightly lower [Zn/Fe] than found in the halo, a low [Y/Fe] at the slightly higher metallicities. The one exception to the similarities is the evolution from low s-process to *r*-process ratios to high *s*-process–to–*r*-process ratios seen in Fornax, Carina, and Sculptor and not in Leo, Draco, and Ursa Minor (unfortunately no Eu abundances were determined by SCS01 for Sextans). This single difference is likely due to a star formation history which does not seem to be linked in any obvious fashion to galaxy mass since Fornax has the largest mass out of this sample and Carina and Sculptor are some of the least massive. Despite this lingering question it is comforting that all of these dSph have very similar intermediate chemical evolutionary histories.

Combining the Sagittarius dSph samples into a single picture (Bonifacio et al. 2000; Smecker-Hane & McMilliam 2002) reveals a galaxy that seems to be intermediate between the Galactic halo and the dSph's in this paper. The metal-poor stars ($[Fe/H] \sim -1.5$) in this paper and SCS01 exhibit slightly enhanced [α/Fe] (defined as the average of [Si/Fe], [Ca/Fe] and [Ti/Fe]) but less than the ratios seen in the Galactic halo. For the metal-poor stars in the Sagittarius dSph, [α/Fe] are slightly higher. But, as mentioned earlier, the [Ca/Fe] and particularly [Ti/Fe] abundances may not be good indicators of the relative contribution of SNe II to SNe Ia since some models of both types of SNe produce both Si, Ca, and Ti in reasonably similar amounts (see Woosley & Weaver 1995 and Table 3 in Iwamoto et al. 1999).

It should be noted that one of the three Smecker-Hane & McWilliam metal-poor stars exhibits a deep mixing abundance pattern. However, no metal-poor dSph stars in SCS01 or this work show a deep mixing abundance pattern.

The metal-rich stars in the Sagittarius dSph ($[Fe/H] \sim -0.5$) exhibit solar-like [α/Fe] and slightly enhanced s-process to *r*-process ratios of heavy elements. These metal-rich stars also exhibit a large deficiency of Al, Na, Ni, and Y. Again, the metal-rich stars share some similarities to the Nissen & Shuster (1997) anomalous stars. There is little overlap between the metal-rich stars in the Sagittarius dSph and the other published dSph abundances though; only the one star in our sample, Fnx 21, is as metal-rich, but it may be an anomalous *s*-process–rich mass-transfer star (see above). Comparisons between the Sagittarius dSph and the other dSph will have to wait until larger surveys of the metal-poor Sagittarius dSph and the metal-rich other dSph's are conducted.

10. SUMMARY

Certain abundance patterns appear to be very similar between the four dwarf spheroidal galaxies studied here (the Sculptor, Fornax, Leo I, and Carina dwarf spheriodals) and the others examined in the literature (the Ursa Minor, Draco, Sextants, and Sagittarius dwarf spheriodals). These include

1. Galactic halo-like abundances for the iron-group elements, in particular [Sc/Fe], [Cr/Fe], [Co/Fe], and [Ni/Fe]. In addition, [Mn/Fe] is halo-like in all the dSph stars.
2. The most metal-poor dSph stars, with $[Fe/H] < -1$, show halo-like *s*- and *r*-process abundance patterns and [Cu/Fe] abundances. The only exception is the first-peak *s*-process element, Y, where [Y/Fe] is lower than in the halo.
3. The most metal-poor dSph stars, with $[Fe/H] < -1$, show lower [Zn/Fe] abundance ratios than the Galactic halo stars.
4. None of the stars in the dSphs show the deep mixing abundance pattern (a possible exception may be one star in Sagittarius). For example, all of the dSph stars with $[Fe/H] < -1$ show a very low Na abundance, with $[Na/Fe] \sim -0.4$.

The α-element abundance patterns are not similar between the dSphs though. The [α/Fe] ratio can vary from galaxy to galaxy and can vary with metallicity in an individual galaxy. Specifically, Carina shows a wide dispersion in the [α/Fe] ratios at a given metallicity, which we interpret in terms of its bursting star formation history. Sculptor and Leo I show a slightly declining α abundance pattern with increasing metallicity, as do Sextants, Ursa Minor, and Sagittarius. Fornax and Draco show a roughly constant α abundance over the metallicites sampled. The α/Fe ratios in the dSph stars continue to be lower than seen in Galactic halo stars of similar metallicity; thus, we remain in agreement with SCS01, that the majority of the Galactic halo cannot have formed from disrupted dSph systems. However, similarities in the [Ni/Fe] and [Na/Fe] abundances with high-velocity halo stars from Nissen & Schuster (1997) may suggest that as much as 50% of the metal-*rich* halo is comprised of dSph stars.

Despite the generally halo-like *s*- and *r*-process abundances in the metal-poor stars (above), not every dSph exhibits the same evolution in the *s*- and *r*-process abundance pattern. Carina, Sculptor, and Fornax show a rise in the *s*-/*r*-process ratio with increasing metallicity, evolving from a pure *r*-process ratio to a solar-like *s*- and *r*-process ratio. On the other hand, Leo I, Draco, and Ursa Minor appear to show an *r*-process–dominated ratio over the range in metallicities sampled. Again, we attribute this to differences in the star formation histories of these galaxies.

The dSph abundances place new constraints on nucleosynthetic origins of several elements. We find that [Cu/Fe] and [Cu/α] are flat over a large range in metallicity in all of the dSph stars. We take these abundance ratios in combination with the known age spread in several of the dSphs as evidence for a metallicity-dependent SN (Ia or II) yield for Cu. The same is found for Mn. Also, we attribute differences in the evolution of [Y/Fe] in the dSph stars versus the halo stars to a very weak AGB or SN Ia yield of Y (especially compared with Ba). That a lower and flatter Ba/Y ratio is seen in the halo is a result of the pattern being erased by the large metallicity dispersion in the halo (as described by McWilliam 1997). If Zn also has a small component that is linked to the production of the first *s*-process elements, then the slight underabundance of Zn might be linked to the underabundances in Y.

We thank the Paranal Observatory staff for excellent support we received during both of our visitor runs. E. T.

gratefully acknowledges support from a fellowship of the Royal Netherlands Academy of Arts and Sciences, and PATT travel support from University of Oxford. K. A. V. would like to thank the National Science Foundation for support through a CAREER award, AST 99-84073. We thank Sonya M. Clarkson, Christina M. Blank, Fitih M. Mohammed, and Leah E. Simon for their assistance with the line measurements and the atmospheric analyses. We thank A. McWilliam for useful discussions and an invaluable review article.

REFERENCES

Alcaino, G. 1975, A&AS, 22, 193
———. 1977, A&AS, 29, 9
Alcaino, G., & Liller W. 1980, AJ, 85, 1330
Alonso, A., Arribas, S., & Martínez-Roger, C. 1999, A&AS, 140, 261
———. 2001, A&A, 376, 1039
Arlandini, C., Kappeler, F., Wisshak, K., Gallino, R., Lugaro, M., Busso, M., & Straniero, O. 1999, ApJ, 525, 886
Asplund, M., & Garcia Perez, A. E. 2001, A&A, 372, 601
Ballester, P., Dorigo, D., Disaro, A., Pizarro de La Iglesia, J. A., & Modigliani, A. 2000, in ASP Conf. Proc. 216, Astronomical Data Analysis Software and Systems IX, ed. N. Manset, C. Veillet, & D. Crabtree (San Francisco: ASP), 461
Bell, R. A. 1985, PASP, 97, 219
Bessell, M. S. 1986, PASP, 98, 1303
———. 1990, PASP, 102, 1181
Biehl, D. 1976, Ph.D. thesis, Univ. Kiel
Bonifacio, P., Hill, V., Molaro, P., Pasquini, L., Di Marcantonio, P., & Santin, P. 2000, A&A, 359, 663
Booth, A. J., Shallis, M. J., & Wells, M. 1983, MNRAS, 205, 191
Buonanno, R., Corsi, C. E., Castellani, M., Marconi, G., Fusi Pecci, F., & Zinn, R. 1999, AJ, 118, 1671
Burris, D. L., Pilachowski, C. A., Armandroff, T. E., Sneden, C., Cowan, J. J., & Roe, H. 2000, ApJ, 544, 302
Cardelli, J. A., Clayton, G. C., & Mathis, J. S. 1989, ApJ, 345, 245
Cayrel, R. 1988, in IAU Symp. 132, The Impact of Very High S/N Spectroscopy on Stellar Physics, ed. G. Cayrel de Strobel & M. Spite (Dordrecht: Kluwer), 345
Clayton, D. D. 1988, MNRAS, 234, 1
Da Costa, G. S. 1984, ApJ, 285, 483
Cunha, K., Smith, V. V., Suntzeff, N. B., Norris, J. E., Da Costa, G. S., & Plez, B. 2002, AJ, 124, 379
Dean, J. F., Warren, P. R., & Cousins, A. W. J. 1978, MNRAS, 183, 569
Dekker, H., D'Odorico, S., Kaufer, A., Delabre, B., & Kotzlowski, H. 2000, Proc. SPIE, 4008, 534
Dohm-Palmer, R. C., Mateo, M., Olszewski, E., Morrison, H., Harding, P., Freeman, K. C., & Norris, J. 2000, AJ, 120, 2496
Dolphin, A. 2002, MNRAS, 332, 91
Edvardsson, B., Andersen, J., Gustafsson, B., Lambert, D. L., Nissen, P. E., & Tomkin, J. 1993, A&A, 275, 101
Fulbright, J. P. 2000, AJ, 120, 1841
———. 2002, AJ, 123, 404
Fulbright, J. P., & Kraft, R. P. 1999, AJ, 118, 527
Gallart, C., Freedman, W. L., Aparicio, A., Bertelli, G., & Chiosi, C. 1999, AJ, 118, 2245
Gibson, B. K. 1998, ApJ, 501, 675
Gilmore, G., & Wyse, R. F. G. 1991, ApJ, 367, L55
Green, E. M., Demarque, P., & King, C. R. 1987, The Revised Yale Isochrones and Luminosity Functions (New Haven: Yale Univ. Obs.)
Gratton, R. G. 1989, A&A, 208, 171
Gratton, R. G., & Sneden, C. 1988, A&A, 204, 193
———. 1991, A&A, 241, 501
———. 1994, A&A, 287, 927
Grevesse, N., & Sauval, A. J. 1998, Space Sci. Rev., 85, 161
Gustafsson, B., Bell, R. A., Ericksson, K., & Norlund, A. 1975, A&A, 42, 407
Harris, W. E. 1996, AJ, 112, 1487
———. 1975, ApJS, 29, 397
Helmi, A., White, S. D. M., de Zeeuw, P. T., & Zhao, H. 1999, Nature, 402, 53
Hernandez, X., Gilmore, G., & Valls-Gabaud, D. 2000, MNRAS, 317, 831
Hill, V. 2003, in preparation
Hodge, P. W. 1965, ApJ, 142, 1390
Hoffman, R. D., Woosley, S. E., Fuller, G. M., & Meyer, B. S. 1996, ApJ, 460, 478
Hurley-Keller, D., Mateo, M., & Nemec, J. 1998, AJ, 115, 1840
Ibata, R. A., Gilmore, G., & Irwin, M. J. 1994, Nature, 370, 194
Ibata, R., Irwin, M., Lewis, G., Ferguson, A. M. N., & Tanvir, N. 2001, Nature, 412, 49
Ibata, R. A., Wyse, R. F. G., Gilmore, G., Irwin, M. J., & Suntzeff, N. B. 1997, AJ, 113, 634
Iwamoto, K., Brachwitz, F., Nomoto, K., Kishmoto, N., Umeda, H., Hix, W. R., & Thielemann, F. 1999, ApJS, 125, 439
Kaluzny, J., Kubiak, M., Szymanski, M., Udalski, A., Krzeminski, W., & Mateo, M. 1995, A&AS, 112, 407
Kinman, T. D., & Kraft, R. P. 1980, AJ, 85, 415
Klypin, A., Wilkinson, M. I., Evans, N. W., Gilmore, G., & Frayn, C. 2002, MNRAS, 330, 792
Koch, A., & Edvardsson, B. 2002, A&A, 381, 500
Kraft, R. P. Sneden, C., Langer, G. E., & Prosser, C. F. 1992, AJ, 104, 645
Kraft, R. P. Sneden, C., Langer, G. E., & Shetrone, M. D. 1993, AJ, 106, 1490
Kraft, R. P. Sneden, C., Langer, G. E., Shetrone, M. D., & Bolte, M. 1995, AJ, 109, 2586
Kraft, R. P., Sneden, C., Smith, G. H., Shetrone, M. D., Langer, G. E., & Pilachowski, C. A. 1997, AJ, 113, 279
Kupka, F., Piskunov, N., Ryabchikova, T. A., Stempel, H. C., & Weiss, W. W. 1999, A&AS, 138, 119
Kurucz, R. L. 1993, CD-ROM 13, ATLAS9 Stellar Atmosphere Programs and 2 km/s Grid (Cambridge: Smithsonian Astrophys. Obs.)
Lambert D. L. 2001, in Oxygen Abundances in Old Stars and Implications to Nucleosynthesis and Cosmology, ed. B. Barbuy (Dordrecht: IAU), in press
Lawler, J. E., Bonvallet, G., & Sneden, C. 2001a, ApJ, 556, 452
Lawler, J. E., Wickliffe, M. E., Den Hartog, E. A., & Sneden, C. 2001b, ApJ, 563, 1075
Majewski, S. R., Patterson, R. J., Dinescu, D. I., Johnson, W. Y., Ostheimer, J. C., Kunkel, W. E., & Palma, C. 2000, in The Galactic Halo: From Globular Cluster to Field Stars, ed. A. Noels, P. Magain, D. Caro, E. Jehin, G. Parmentier, & A. A. Thoul (Liège: Inst. d'Astrophys.), 619
Massey, P. 2002, ARA&A, in press
Mateo, M. 1998, ARA&A, 36, 435
Mateo, M., Olszewski, E. W., Vogt, S. S., & Keane M. J. 1998, AJ, 116, 2315
Mateo, M., Olszewski, E. W., Pryor, C., Welch, D. L., & Fischer, P. 1993, AJ, 105, 510
Mateo, M., Olszewski, E. W., Welch, D. L., Fischer, P., & Kunkel, W. 1991, AJ, 102, 914
Mathews, G. J., Bazan, G., & Cowan, J. J. 1992, ApJ, 391, 719
Matteucci, F., Raiteri, C. M., Busso, M., Gallino, R., & Gratton, R. 1993, A&A, 272, 421
McWilliam, A. 1997, ARA&A, 35, 503
———. 1998, AJ, 115, 1640
McWilliam, A., Preston, G. W., Sneden, C., & Searle, L. 1995, AJ, 109, 2757
Mighell, K. J. 1990, A&AS, 82, 1
Minniti, D., Geisler, D., Peterson, R., & Claria, J. J. 1993, ApJ, 413, 548
Monkiewicz, J., et al. 1999, PASP, 111, 1392
Moore, B., Ghigna, S., Lake, G., Quinn, T., Stadel, J., & Tozzi, P. 1999, ApJ, 524, L19
Mould J., & Aaronson M. 1983, ApJ, 273, 530
Nakamura, T., Umeda, H., Nomoto, K., Thielemann, F.-K., & Burrows, A. 1999, ApJ, 517, 193
Newberg, H. J., et al. 2002, ApJ, 569, 245
Nissen, P. E., & Schuster, W. J. 1997, A&A, 326, 751
Pancino, E., Pasquini, L., Hill, V., Ferraro, F. R., & Bellazzini, M. 2002, ApJ, 568, L101
Primas, F., Brugamyer, E., Sneden, C., King, J. R., Beers, T. C., Boesgaard, A. M., & Deliyannis, C. P. 2000, in The First Stars, ed. A. Weiss, T. Abel, & V. Hill (New York: Springer), 51
Qian, Y. Z. 2002, ApJ, 569, L103
Qian, Y. Z., & Wasserburg, G. J. 2002, ApJ, 567, 515
Queloz, D., Dubath, P., & Pasquini, L. 1995, A&A, 300, 31
Salpeter, E. E. 1955, ApJ, 121, 161
Samland, M. 1998, ApJ, 496, 155
Schlegel, D. J., Finkbeiner, D. P., & Davis, M. 1998, ApJ, 500, 525
Schweitzer, A. E., Cudworth, K. M., Majewski, S. R., & Suntzeff, N. B. 1995, AJ, 110, 2747
Shetrone, M. D. 1996, AJ, 112, 1517
Shetrone, M. D., Bolte, M., & Stetson, P. B. 1998, AJ, 115, 1888
Shetrone, M. D., Côté, P., & Sargent, W. L. W. 2001, ApJ, 548, 592 (SCS01)
Smecker-Hane, T. A., & McMilliam, A. 2002, ApJ, submitted (astro-ph/0205411)
Smecker-Hane, T. A., Stetson, P. B., Hesser, J. E., & Lehnert, M. D. 1994, AJ, 108, 507
Smith, G. H. 1984, AJ, 89, 801
Smith, G. H., & Dopita, M. A. 1983, ApJ, 271, 113
Sneden, C. 1973, ApJ, 184, 839
Sneden, C., Kraft, R. P., Prosser, C. F., & Langer, G. E. 1991, AJ, 102, 2001
Sneden, C., Kraft, R. P., Shetrone, M. D., Smith, G. H., Langer, G. E., & Prosser, C. F. 1997, AJ, 114, 1964
Stephens, A. 1999, AJ, 117, 1771
Truran, J. W. 1981, A&A, 97, 391
Timmes, F., Woosley, S. E., & Weaver, T. A. 1995, ApJS, 98, 617

Tolstoy, E., Irwin, M. J., Cole, A. A., Pasquini, L., Gilmozzi, R., & Gallagher, J. S. 2001, MNRAS, 327, 918
Tolstoy, E., Venn, K., Shetrone, M., Primas, F., Hill, V., Kaufer, A., & Szeifert, T. 2003, AJ, 125, 707 (Paper II)
Tsujimoto, T., & Shigeyama, T. 2001, ApJ, 561, L97
Umeda, H., & Nomoto, K. 2002, ApJ, 565, 385
van den Bergh, S. 2000, ApJ, 530, 777
Wallerstein, G., et al. 1997, Rev. Mod. Phys., 69, 995
White, S. D., & Rees, M. 1978, MNRAS, 183, 341
Woosley, S. E., & Weaver, T. A. 1995, ApJS, 101, 181
Yi, S., Demarque, P., Kim, Y.-C., Lee, Y.-W., Ree, C.-H., Lejeune, T., & Barnes, S. 2001, ApJS, 136, 417